Explaining monthly precipitation anomalies in northwestern South America by integrating vertical dynamics and energetics

Jose Obregon-Yataco[1]

[1]Ciencias de la Atmósfera, Hidrósfera y Cambio Climático, Instituto Geofísico del Perú, Lima, Peru

Correspondence: Jose Obregon-Yataco (jobregyat@gmail.com)

Abstract. Northwestern South America (NWSA), a region critically important for monitoring coastal El Niño and La Niña events, receives its maximum cumulative precipitation in February-March. Thermodynamic indices alone, often fail to explain observed precipitation anomalies because they neglect the influence of large-scale environmental dynamics. To bridge this gap, a low-frequency climate index called Buoyancy Work Rate (BWR) is proposed, which quantifies the rate of conversion from potential to kinetic energy by coupling local thermodynamic instability with vertical motion (ω) forced by large-scale dynamics. The BWR is calculated by vertically integrating the product of parcel buoyancy (ΔT) and ω from the surface to the 100 hPa level. Statistical evaluation between 1981 and 2024 demonstrates that BWR outperforms established indices in spatial correlation, RMSE, and F1-scores, particularly for extreme precipitation events. Physically, the index explains how variations in vertical motion profiles modulate precipitation outcomes across events with similar instability, effectively explaining the contrasting impacts of the 2016, 2017, and 2023 El Niño events. Furthermore, since BWR capture primarily on large-scale vertical motions, which typically exhibit higher predictability in climate models than vertical humidity profiles, the BWR emerges as a robust candidate for future forecasting applications.

1 Introduction

The El Niño-Southern Oscillation (ENSO) is one of the main drivers of global climate variability, altering weather patterns worldwide through its irregular oscillation between El Niño, La Niña, and neutral phases (McPhaden et al., 2006; Wang et al., 2016). Northwest South America (NWSA) is a region of critical scientific importance for monitoring these events, particularly coastal El Niño events, while also being exceptionally vulnerable to their hydroclimatic and socioeconomic impacts (Callahan and Mankin, 2023; Poveda et al., 2025).

Although sea surface temperature (SST) in the Niño 1+2 region has a known critical threshold that can trigger deep convection (Takahashi and Martínez, 2017; Takahashi et al., 2018), SST alone has proven to be an insufficient predictor of precipitation (Sulca and Takahashi, 2025). In fact, studies have shown that above a certain SST threshold (approximately 28 °C), the relationship between temperature and convection breaks down, and convection becomes more strongly controlled by large-scale vertical motions (Lau et al., 1997; Bony et al., 1997).

Estimating precipitation anomalies remains a significant challenge, as it requires understanding deep moist convection, the process of vertical heat and moisture transport that drives tropical climates (Houze, 2004). This process is governed by a

complex bidirectional interaction between local thermodynamic instability, which provides the potential energy for storms, and large-scale atmospheric dynamics, which provides the necessary trigger to release that energy (Lau et al., 1997; Bony et al., 1997). For decades, the conventional metric for assessing this potential has been Convective Available Potential Energy (CAPE), a purely thermodynamic index (Emanuel, 1994). However, CAPE has been shown to be a poor predictor of precipitation in the tropics. Its fundamental limitation is that it quantifies potential instability without considering the dynamic forcing (i.e., large-scale updrafts) required to initiate convection. This leads to a high rate of false positives: the simultaneous presence of a finite CAPE and infrequent deep convection is a common state in the tropics, often attributed to convective inhibition (CIN) or large-scale dynamic subsidence (Williams and Renno, 1993; DeMott and Randall, 2004). Conversely, large-scale vertical motion (ω) has been shown to be the main controlling factor, explaining 45-55% of the variance in tropical convection, much more than local SST, which explains only 15-20% (Lau et al., 1997).

This disconnect between thermodynamic potential and realized convection is particularly evident in the complex ocean-atmosphere interactions of the eastern Pacific. The 2017 and 2023 Coastal El Niño events produced extreme rainfall along the coast. However, the 2015-2016 global El Niño, despite its large magnitude in SST over the central Pacific, did not produce comparable severe precipitation impacts on the South American coast (Paek et al., 2017). This discrepancy underscores the critical role of regional dynamics in modulating thermodynamic instability (Sulca et al., 2017; Sanabria et al., 2019). To rigorously distinguish these regimes, Takahashi et al. (2011) proposed the orthogonal C and E indices, characterizing Central Pacific (Modoki) and extreme Eastern Pacific warming, respectively. Complementing these, Sulca and Takahashi (2025) introduced the $CPTICZ$ and $EPTICZ$ atmospheric indices, which quantify the zonal and meridional displacements of the Intertropical Convergence Zone (ITCZ), respectively, providing a more direct measure of the convective response to oceanic forcing.

Atmospheric dynamics, including processes such as low-level convergence, high-level divergence, and vertical transport, are fundamental. These physical mechanisms occur on timescales of minutes to hours (high frequency) (Riehl, 1958; Zipser, 2003; Houze, 2004). Many indices that attempt to simplify these processes were developed to monitor deep convection at synoptic (daily) scales (Showalter, 1953; George, 2014; Gálvez, 2016). However, this study is interested in monthly averages (low frequency) to isolate robust climate signals from the "noise" of daily meteorological fluctuations (Trenberth, 1997; Sobel and Bretherton, 2000; Back and Bretherton, 2006). The average of daily conditions within a month reveals the dominant state of the troposphere, whether favorable or unfavorable for the development of deep convection. Therefore, in this study, synoptic indices were adapted for use at a climatic (monthly) scale, and a new climatic index was proposed that links thermodynamic potential with realized convection, which could be used to estimate monthly precipitation over the NWSA.

The main objective of this research was to develop, validate, and apply the Buoyancy Work Rate (BWR) index as a diagnostic tool to explain and estimate monthly precipitation patterns in northwestern South America (NWSA). The BWR quantifies the rate at which buoyancy potential energy is converted into updraft kinetic energy by vertically integrating the product of vertical velocity (ω) and parcel buoyancy (ΔT). In doing so, the BWR goes beyond simply measuring potential and instead quantifies active, ongoing convection. This index was applied to analyze anomalous precipitation events from 1981 to 2024 across the NWSA.

To validate the performance of the Buoyancy Work Rate (BWR), it was compared with other indices tested in the NWSA. For example, the CAPE index and the Galvez-Davison index (GDI) (Gálvez, 2016) were tested by Rivas Quispe et al. (2024), and the asymmetric index (Ia) and the double ITCZ index (Id), proposed by Yu and Zhang (2018), were adapted and tested by Aliaga-Nestares et al. (2023). However, none of these indices explicitly considers vertical motion as a core component. The GDI does not contain any explicit kinematic component, and the Ia and Id indices are based on precipitation anomalies, not atmospheric dynamics. Therefore, the authors believe that the BWR index could be a valuable tool for explaining why some precipitation events, which were assumed to be extreme based solely on local thermodynamics, ended up being neutralized by large-scale subsidence in some important layer of the troposphere.

2 Data

Monthly mean air temperature (T_a), relative humidity (RH), and zonal, meridional, and vertical wind components were obtained from the ERA5 reanalysis dataset (Hersbach et al., 2020). These data were utilized for the period 1981-2024 across 27 vertical pressure levels ranging from 1000 to 100 hPa, with a spatial resolution of 0.25°. To validate the proposed climate index, independent monthly precipitation datasets were employed: the RAIN4PE product (Fernandez-Palomino et al., 2022) for the 1981-2015 period, and the PISCO product (Peruvian Interpolated Data of the SENAMHI's Climatological and Hydrological Observations) (Aybar et al., 2019) for the 1981-2024 period. It is important to note that the stable version of PISCO, which incorporates both manual and automatic quality control (Aybar et al., 2019), is available only for the 1981-2016 period; consequently, the unstable version, which undergoes only automatic quality control, was utilized for the 2017-2024 period. Due to RAIN4PE only has data until 2015 and the uncertainty of PISCO increases from 2017 onwards, the monthly precipitation from ERA5 (Hersbach et al., 2020), which provides coverage over both land and ocean, was used to evaluate similarities among the precipitation products, as a form of data triangulation to increase the credibility of precipitation anomaly behavior. Finally, monthly sea surface temperature (SST) was also utilized to provide context for the identified rainiest and driest events.

3 Study Area

Two interest areas were defined, the NWSA (18.95°S-1.95°N, 81.95°W-67.05°W) and the NWSA adjacent to Niño 1+2 (81.25°W-78.5°W, 8°S-0.75°N) (Fig. A3). The Fig. 1 shows the precipitation climatology (1981-2015) from ERA5 averaged over this second area. The climatology shows that February and March are the rainiest months of the year, this February-March peak is a coupling window, where dynamic relaxation (trade winds) and thermodynamic instability (SST) come into phase (Takahashi, 2004; Poveda et al., 2006; Adachi et al., 2018; Peng et al., 2024).

4 Identification and analysis of rainiest and driest events

First, the driest and rainiest March events were identified by averaging precipitation over the NWSA region adjacent to Niño 1+2 (Fig. A3) and calculating the precipitation anomalies from the ERA5 dataset, using the 1981-2024 median as the clima-

tological baseline. Two arbitrary thresholds were defined: -20 mm month^{-1} to detect the driest events and 60 mm month^{-1} to detect the rainiest events.

Second, the vertical motion was analyzed through latitudinal and longitudinal cross-sections. The longitude of 80°W was identified as the core of vertical ascent; subsequently, from this cross-section, the latitude of 5°S was identified as the core of vertical ascent over the NWSA adjacent to Niño 1+2. This analysis allowed for the identification of subsidence and convective layers, as well as the specific levels at which convection was initiated and terminated.

5 Buoyancy Work Rate Calculation

The dew point temperature (T_d) was calculated from the relative humidity using the equation proposed by Bolton (1980). Using the surface T_d and air temperature (T_a) values, the temperature of the air parcel was computed. Subsequently, the difference between the parcel temperature and the environmental air temperature profiles was determined, yielding the parcel buoyancy (ΔT) for every grid point within the NWSA domain. Profile plots were then generated at the core of vertical ascent (5°S, 80°W), identified in Section 4. In these plots, the ΔT, vertical velocity (ω), and $-\omega\Delta T$ profiles were compared to identify common characteristics associated with the driest and rainiest events.

Then, the $-\omega\Delta T$ product was vertically integrated from the surface to 100 hPa with respect to the natural logarithm of pressure ($d\ln P$), as shown in Eq. (1). Only positive areas were included in the integration because the focus was on the kinetic energy required to trigger deep convection. The result of this integration is defined as the Buoyancy Work Rate (BWR) index. Finally, plots were generated to analyze the spatial distribution of the BWR for the rainiest and driest events identified in Section 4.

$$BWR = -\int_{sfc}^{100} \omega\Delta T \, d\ln P \tag{1}$$

6 Evaluation of the BWR performance

To evaluate the performance of the Buoyancy Work Rate (BWR), comparisons were made with other indices previously tested in the NWSA. Specifically, the Convective Available Potential Energy (CAPE) and the Gálvez-Davison Index (GDI) were evaluated by Rivas Quispe et al. (2024), while the asymmetric index (I_a) and the double ITCZ index (I_d) were assessed by Aliaga-Nestares et al. (2023). These indices were compared to the BWR by analyzing their similarity to monthly precipitation products. To this end, the spatial distributions of the Pearson correlation coefficient, Root Mean Square Error (RMSE), and F1-score were calculated between the anomalies of the spatial indices (CAPE, BWR, and GDI) and the anomalies of three precipitation products (ERA5, PISCO, and RAIN4PE) across the NWSA for the common period of 1981-2015.

The F1-score was computed for precipitation anomalies classified into three categories: values lower than -5 mm month^{-1}, values greater than 5 mm month^{-1}, and values greater than 60 mm month^{-1}. The F1-score metric is defined as follows:

$$
\begin{aligned}
F1 &= 2 \times \frac{P \times R}{P + R} \\
P &= \frac{TP}{TP + FP} \\
Re &= \frac{TP}{TP + FN}
\end{aligned}
\tag{2}
$$

where P denotes precision, Re denotes recall, TP represents true positives, FP represents false positives, and FN represents false negatives. Values closer to 1 indicate a high degree of similarity between a given climate index and monthly precipitation.

To evaluate the performance of the BWR over the NWSA region adjacent to Niño 1+2, the same climate indices were utilized. However, in this analysis, both the indices and the precipitation products were averaged using only land pixels within the domain defined by 81.25°W-78.5°W and 8°S-0.75°N (Fig. A3). Subsequently, scatterplots were generated, and the Pearson correlation coefficient (R) and RMSE were calculated for the common period of 1981-2015. Additionally, time series plots were constructed to analyze the temporal behavior of both the indices and the precipitation products.

7 Results and Discussion

7.1 Identification and analysis of rainiest and driest events

Monthly precipitation anomalies for March are shown in Fig. 2. Based on the thresholds defined on the Section 4, the years 1983, 1987, 1992, 1998, 2002, 2017, and 2023 were identified as the rainiest events, whereas 1982, 1988, 1995, 2003, 2018, and 2024 were classified as the driest. These observed extremes are associated with coastal El Niño and La Niña phases, as evidenced in Fig. A1. In this figure, positive Sea Surface Temperature (SST) anomalies in the Niño 1+2 region are exhibited during the rainiest years, while negative anomalies are generally observed during the driest ones. An exception is noted for March 2024, which was characterized by slightly cool to neutral conditions near the coast. Consequently, these specific events were selected for further analysis. Additionally, the 2016 event was included in the study due to the prevailing El Niño conditions in the Niño 1+2 region.

7.2 Cross-section analysis in the NWSA adjacent to Niño 1+2

The rainiest events previously identified consistently exhibit air ascent around 80°W and 5°S in the middle to upper troposphere, with the most intense ascent observed during the 1998 El Niño, followed by the 2017 coastal El Niño (Fig. 3k and Fig. 4k). With the exception of the 2002 event, subsidence was observed in the planetary boundary layer (PBL) for all these events, a barrier that the air parcel had to overcome to reach the level of free convection. Conversely, the driest events were characterized by weak ascent near the PBL and subsidence from the middle to upper troposphere around 80°W.

Specifically, the 2016 event showed weak ascent near the PBL around 5°S (Fig. 3j) and around 80°W (Fig. 4j), but this was accompanied by subsidence in the middle troposphere (Fig. 4j), which could have partially neutralized heavy rainfall. This contrasts with the 2017 event, which produced rainfall in Piura, Tumbes, and Lambayeque comparable to the 1983 and 1998 events, and in many regions of northern Peru, historical records were even exceeded (Rodríguez-Morata et al., 2018; Thielen et al., 2023).

7.3 Precipitation spatial distribution in the NWSA

We analyzed the rainiest events (identified previously in the Section 4) and we identified positive anomalies in the NWSA adjacent to Niño 1+2 (Fig. 5), however we can note different spatial patterns, e.g. we identified that when the northwestern positive anomalies are distributed at least until the central coast, almost all the domain was stimulated by deep convection (Fig. 5b,g,h,k,m). Unlike the rest, the 1987, 1992 and 2016 events (Fig. 5c,e,j) were dominated by negative anomalies almost entirely. These events are classified as Central Pacific (CP) or "Modoki" El Niño events, characterized by maximum Sea Surface Temperature (SST) warming confined to the central equatorial Pacific (Niño 3.4) rather than the far eastern coast (Niño 1+2) (Takahashi et al., 2011). This configuration displaces the ascending branch of the Walker Circulation westward, forcing a compensating branch of anomalous subsidence (sinking air) over the NWSA, which inhibits deep convection and rainfall despite the global El Niño conditions (Sulca et al., 2017; Paek et al., 2017).

Sulca et al. (2017) observed results consistent with the strong positive SST anomalies recorded in the central Pacific, which contrasted with the weaker anomalies in the eastern Pacific during the 2016 event. During this period, the southward displacement of the ITCZ was found to be limited. Although displacements were exhibited by the SPCZ, the "atmospheric bridge," which typically connects equatorial warming with the South American coast, was not firmly established (Sulca et al., 2017). The descending branch of the Walker Circulation (subsidence) did not shift sufficiently eastward to be replaced by the ascending branch over the South American coast. Instead, the ascending motion remained anchored to the warming of the Central Pacific, leaving the coast under the influence of relatively stable and dry air compared to the conditions observed in 1998 (Paek et al., 2017). Furthermore, Sanabria et al. (2019) revealed that the 2016 El Niño exhibited an "out-of-phase" atmospheric response where the ITCZ shifted northward and upper-level divergence did not align with the coastal domain, resulting in moisture deficits instead of the surplus observed during "Canonical" or Eastern Pacific events like 1983 or 1998.

The sudden SST warming off the coast of Peru in 2017, which reached approximately 29°C, was driven not by remote Kelvin waves but by a localized relaxation of the trade winds forced by atmospheric teleconnections from the western Pacific (Rossby waves) (Echevin et al., 2018). A specific "atmospheric trigger" was identified by Garreaud (2018), wherein deep convection over Australia triggered a Rossby wave train that weakened the South Pacific High off the coasts of Chile and Peru, thereby facilitating warming in the Niño 1+2 region. The general mechanism is initiated by the generation of a Rossby wave train due to deep convection in the western region of the SPCZ; this system shifts eastward, modulating precipitation regimes in South America (Aguirre-Correa et al., 2025).

Conversely, the driest events were dominated almost entirely by negative anomalies (Fig. 5a,d,i,l), with the exception of 1995 and 2024 (Fig. 5f,n), where the negative anomalies only are confined over the NWSA adjacent to Niño 1+2.

A statistically significant correlation was found between monthly precipitation from ERA5 and PISCO (a), as well as RAIN4PE (b), within the NWSA (Fig. 6). In both products, the highest values ($R > 0.7$) were observed adjacent to the Niño 1+2 region, specifically between Peru and Ecuador. However, a slightly greater magnitude was generally exhibited by the RAIN4PE product compared to ERA5. This last is likely attributable to the fact that ERA5 is utilized as one of the input datasets in the calculation of the RAIN4PE product (Fernandez-Palomino et al., 2022).

7.4 Vertical structure analysis

Vertical profiles of ΔT, ω and $-\omega\Delta T$ at (80°W,5°S) for the rainiest and driest events identified in Section 4 are shown in the Fig. 7. The rainiest events (identified in Section 4) were analyzed, with a focus placed on the positive area between the surface and 100 hPa. The area bounded by the green curve and the 0°K temperature represents the Buoyancy Work Rate (BWR) index, while the area formed by the red curve represents the CAPE between the Level of Free Convection (LFC) and the Equilibrium Level (EL). It is noted that the BWR can be greater or lower than the CAPE, depending on the ω profile.

A consistent pattern was observed across the rainiest events, characterized by a sustained ascending ω profile. This is consistent with the air ascent at (80°W, 5°S) identified in Fig. 3 and Fig. 4, with the exception of 1992 and 2016; the latter exhibited significant subsidence at mid-levels (blue line in Fig. 7j). Furthermore, the 1998 El Niño event exhibited the strongest BWR, and the 2017 Coastal El Niño presented a stronger BWR than even the 1983 El Niño. Although the parcel buoyancy (ΔT) values for 1983, 1998, and 2017 were similar, the primary differentiator was the large-scale ω. This indicates that the troposphere in March 1998 provided stronger forcing than in 1983, while March 2017 was forced similarly to 1998. Subsidence was observed in the PBL for all these events. Despite the air parcel in March 1983 requiring less energy to overcome its CIN than in 1998 to reach the level of free convection, the 1983 event produced a lower BWR due to weaker upward ω values. Furthermore, all these rainiest events were accompanied by warm SST conditions (Fig. A1) in the Niño 1+2 region. Positive SST anomalies in this region define the Coastal El Niño and are critical for destabilizing the local atmosphere by neutralizing the trade winds and enhancing lower-tropospheric moisture, thereby facilitating deep convection (Takahashi and Martínez, 2017; Echevin et al., 2018).

Conversely, the driest events shared significant subsidence at mid-levels (i.e., $\omega > 0$ around 600 hPa). This monthly-scale subsidence could be originated from planetary circulations, such as the Walker Circulation, where a strengthened descending branch suppresses vertical motion over the region (Sulca, 2021). These results are consistent with Lau et al. (1997), who indicated that large-scale vertical motions largely control tropical convection. In most of these driest events, cold SST conditions were observed (Fig. A1) in the Niño 1+2 region. Negative SST anomalies enhance the stability of the coastal boundary layer and strengthen the subsidence inversion, effectively inhibiting the development of deep convection (Takahashi, 2004; Rudloff et al., 2025). Although the dynamics of the central Pacific were not analyzed herein, as in Sulca and Takahashi (2025), it is established that warming or cooling in that region affects the Walker Circulation, which can induce teleconnected monthly-scale subsidence anomalies in the NWSA during the driest events (Takahashi and Dewitte, 2016; Sulca et al., 2017).

7.5 BWR performance

The BWR anomalies calculated for the rainiest and driest events, identified in Section 4, are shown in Fig. 8. Positive BWR values were observed along the coast between Peru and Ecuador during the rainiest events. This finding is consistent with the cross-section analysis, the distribution of precipitation anomalies, the vertical structure (Sections 7.2 to 7.4), and the SST in the Niño 1+2 region (Fig. A1b,c,e,g,h,k,m).

The diversity of the rainiest events is evident. For instance, rainfall events were observed in the NWSA adjacent to Niño 1+2, where conditions favorable for deep convection activation were limited to the area between the northern coast of Peru and Ecuador. Their spatial distribution patterns are similar to those of the precipitation anomalies (Figs. 5 and 8 c,e,j). Conversely, another group of rainiest events was identified in which favorable deep convection conditions extended across nearly the entire Ecuadorian territory and parts of Colombia and Brazil, exhibiting distributions similar to the precipitation anomalies (Figs. 5 and 8 b,g,h,k).

Although the 2016 event was not identified as a rainiest event in Section 4, it was included in the analysis due to its association with the 2015-2016 global El Niño, which is corroborated by the warming depicted in Fig. A1j. Neutral BWR values were observed along the coast between Peru and Ecuador for this event (Fig. 8j). These findings suggest that deep convection driven by SST warming was suppressed by tropospheric dynamics and energetics. It was demonstrated by Sulca and Takahashi (2025) that the simultaneous correlation between the C index (oceanic index in the central Pacific) and precipitation over the NWSA is not significant during the rainy season. This suggests that remote SST variability in the central Pacific does not simultaneously affect monthly precipitation patterns over this region, unlike the CPTICZ atmospheric index. Furthermore, it was shown by the same authors that the contribution of the atmospheric index EPTICZ was significantly greater than that of the E index (oceanic index in the eastern Pacific), suggesting that atmospheric indices perform better than oceanic indices in predicting precipitation in the NWSA adjacent to Niño 1+2.

Regarding dry events, negative BWR anomalies were observed along the coast and western highlands between Peru and Ecuador. This is consistent with the cross-section analysis (Section 7.2), the vertical structure (Section 7.3), the distribution of precipitation anomalies (Section 7.4), and the SST in the Niño 1+2 region (Fig. A1 a,d,f,i,l,n). A diversity of dry events was also observed. For example, dry events were noted in the NWSA adjacent to Niño 1+2, where unfavorable conditions for deep convection activation were confined to the area between the northern coast of Peru and Ecuador (Fig. 8 a,f,l). However, another group of dry events was identified where these unfavorable conditions extended across almost all of Ecuador and parts of Colombia and Brazil (Fig. 8 d,i,n).

The spatial distribution of the correlation between the anomalies of the convective indices and the monthly precipitation anomalies is shown in Fig. 9. In general terms, it is observed that BWR and CAPE exhibit stronger correlations over the NWSA adjacent to Niño 1+2. However, CAPE is not consistent over the entire domain, exhibiting numerous non-significant correlation grid points and even negative relationships over the Amazon. This suggests that parcel buoyancy alone is not a sufficient condition for estimating precipitation in this region. Significant correlations were shown by the GDI over the entire domain; however, these values ($R \leq 0.7$) were lower than those of BWR and CAPE adjacent to Niño 1+2. Similarly, Ia and

Id were calculated (Fig. A2), showing the poorest performance with weak and non-significant correlations across almost the entire domain.

The RMSE maps associated with those correlations are presented in Fig. 10. Generally, the lowest RMSE values were observed along the coast, while the highest values were found in the NWSA adjacent to Niño 1+2, the eastern Andes, and the Northern Amazon. F1-score metric values for precipitation anomalies lower than -5 mm month^{-1}, greater than 5 mm month^{-1}, and greater than 60 mm month^{-1} are shown in Figs. 11-13. Overall, the spatial performance is very similar to that previously observed in Figs. 9-10, with the distinction that a slightly better performance was exhibited by the BWR for the NWSA adjacent to Niño 1+2, particularly for extreme precipitation anomaly events greater than 60 mm month^{-1}.

The area exhibiting the best performance in the evaluated metrics was the NWSA adjacent to Niño 1+2 (Fig. A3). Consequently, land values within this area were averaged to obtain a single time series for every climate index and precipitation product. Scatterplots among the standardized anomalies over this area are shown in Fig. 14. Better performance was demonstrated by the BWR index (Fig. A3d-f) compared to the other indices, characterized by the highest R, lowest RMSE, and values well-aligned with the identity function without the need for an offset. Conversely, the poorest performance was shown by Ia and Id (Fig. A3j-o), which is consistent with the lowest R, largest RMSE, and lowest F1-score maps shown in Figs. 9-13[i-o], as well as the unclear relationship between these indices and the rainiest and driest events (Fig. A2).

Time series of monthly standardized anomalies for the three best-performing indices (BWR, CAPE, and GDI) and precipitation products were generated (Fig. 15). The 1982 dry event was more accurately detected by the GDI, while the behavior of the 1983 rainy event was better captured by the BWR. Similarly, the 1987 rainy event was well detected by both the GDI and BWR. The 1988 dry event was better identified by the BWR and GDI, whereas the 1992 rainy event was better detected by the BWR and GDI. Likewise, the 1995 dry event was better detected by the BWR and CAPE. The 1998 rainy event was better captured by the BWR; in this specific case, slightly different behaviors were observed in the PISCO and RAIN4PE products. For the 2002 rainy event, a peak similar to that of the precipitation products was reached by the BWR. During the 2003 dry event, a trough similar to the precipitation products was shown by the BWR. For the 2016 "rainy" event, no similar behavior was observed in any index, as the mean precipitation oscillated between values close to zero. In the 2017 rainy event, a peak similar to the precipitation products was exhibited by the BWR and CAPE. For the 2018 dry event, a trough similar to the precipitation products was reached by the BWR and GDI. In the 2023 rainy event, the indices were very similar during February and March; however, a sudden decline was experienced by PISCO in April, contrary to the indices and even the ERA5 precipitation, which reached their peak in April. Finally, for the 2024 dry event, a peak value very similar to the 2023 event was unexpectedly reached by the PISCO product. This contradicts the results shown by the BWR, CAPE, and ERA5 precipitation, where negative anomalies with a maximum decline in March were observed. While negative anomalies were shown in the northern coast of Peru in Fig. 5, the average could have been affected by high positive anomalies in Ecuador. This contradictory behavior between the indices and the ERA5 and PISCO precipitation suggests that the spatial and temporal consistency of the PISCO data should be manually verified, particularly since 2017, as from that year onwards, only automatic quality control has been applied to the PISCO product.

8 Conclusions

The development of the Buoyancy Work Rate (BWR) index addresses a fundamental limitation in the diagnosis of tropical convection: the decoupling between thermodynamic potential and dynamic realization. By vertically integrating the product of parcel buoyancy (ΔT) and large-scale vertical velocity (ω), the BWR quantifies the rate of energy conversion, effectively filtering out potential instability that is suppressed by large-scale subsidence.

The diagnostic power of the BWR was demonstrated through the analysis of complex climate events in the NWSA adjacent to Niño 1+2, providing physical explanations that thermodynamic indices alone failed to capture. Specifically, the low precipitation observed during the 2016 Global El Niño was attributed to significant subsidence around 600 hPa, which inhibited deep convection despite high sea surface temperatures. Conversely, the extreme precipitation of the 2017 Coastal El Niño was explained by an ω profile with an ascent magnitude comparable to that of the 1998 El Niño, identifying them as dynamically analogous events. Furthermore, the distinctive intensity difference between the 2017 and 2023 events was explained; although both events shared similar instability profiles, the 2023 event exhibited a weaker vertical motion magnitude in the middle troposphere, resulting in less intense precipitation.

Statistically, the BWR demonstrated superior performance compared to established indices such as CAPE, GDI, Ia, and Id. In the NWSA region adjacent to Niño 1+2, the BWR exhibited the highest spatial correlations, the lowest RMSE, and the highest F1-scores, particularly for extreme precipitation anomalies greater than 60 mm month^{-1}. This indicates that the inclusion of the vertical velocity profile is essential for the accurate detection of extreme events in this dynamically sensitive region.

Finally, a key advantage of the BWR lies in its formulation. Unlike the GDI, which relies on the vertical distribution of humidity, a variable characterized by high discontinuity and sensitivity to sub-grid parameterization schemes, the BWR depends primarily on the air temperature and ω profiles. Since large-scale dynamical circulations and mass fields typically exhibit higher predictability limits in numerical models than moisture fields, the BWR is proposed as a robust candidate for future forecasting applications, offering a physically consistent link between large-scale climate forcing and local precipitation impacts.

Finally, one distinctive characteristic of the BWR is that it does not explicitly incorporate the humidity, unlike the GDI which requires mixing ratios at multiple levels. Despite this apparent limitation, BWR demonstrated superior performance compared to GDI in the NWSA adjacent to Niño 1+2. The current formulation of the BWR index relies solely on the vertical profiles of air temperature and ω from the surface to 100 hPa, alongside the surface dew point temperature. From a climate modeling perspective, large-scale dynamical circulations, such as the Walker ciculation with its ascending and descending branches, typically exhibit higher predictability limits in the Eastern Pacific than the vertical distribution of humidity, which is highly discontinuous and sensitive to sub-grid parameterization schemes (John and Soden, 2007; Emmenegger et al., 2024). This predictive advantage supports the potential of the BWR as a robust candidate for forecasting applications in future research.

Code and data availability. PISCO V2.1 dataset is available at https://iridl.ldeo.columbia.edu/SOURCES/.SENAMHI/.HSR/.PISCO/index.html; RAIN4PE at https://datapub.gfz-potsdam.de/download/10.5880.PIK.2020.010enouiv/; ERA5 reanalysis data at https://cds.climate.copernicus.eu/datasets

Author contributions. All authors designed the study, analyzed and interpreted the results, and wrote and reviewed the manuscript.

Competing interests. The authors declare no competing interests.

Acknowledgements. The authors extend their gratitude to Ricardo Gutierrez for support with recommendations and suggestions.

References

Adachi, N., Takemura, K., Sato, H., and Kamiguchi, K.: A case study of coastal El Niño event in early 2017, in: 98th American Meteorological Society Annual Meeting, AMS, 2018.

Aguirre-Correa, F., Bollasina, M., Garreaud, R., and Suárez, F.: Rossby waves as key drivers of the South American Monsoon high-frequency variability, Atmospheric Research, 326, 108 206, https://doi.org/10.1016/j.atmosres.2025.108206, 2025.

Aliaga-Nestares, V., Rodriguez-Zimmermann, D., and Quispe-Gutiérrez, N.: Behavior of the ITCZ second band near the Peruvian coast during the 2017 coastal El Niño, Atmósfera, 36, 23–39, 2023.

Aybar, C., Fernández, C., Huerta, A., Lavado, W., Vega, F., and Felipe-Obando, O.: Construction of a high-resolution gridded rainfall dataset for Peru from 1981 to the present day, Hydrological Sciences Journal, 65, 770–785, https://doi.org/10.1080/02626667.2019.1649411, 2019.

Back, L. and Bretherton, C.: Geographic variability in the export of moist static energy and vertical motion profiles in the tropical Pacific, Geophysical research letters, 33, 2006.

Bolton, D.: The Computation of Equivalent Potential Temperature, Monthly Weather Review, 108, 1046–1053, https://doi.org/10.1175/1520-0493(1980)108<1046:tcoept>2.0.co;2, 1980.

Bony, S., Lau, K.-M., and Sud, Y. C.: Sea Surface Temperature and Large-Scale Circulation Influences on Tropical Greenhouse Effect and Cloud Radiative Forcing, Journal of Climate, 10, 2055–2077, https://doi.org/10.1175/1520-0442(1997)010<2055:sstals>2.0.co;2, 1997.

Callahan, C. W. and Mankin, J. S.: Persistent effect of El Niño on global economic growth, Science, 380, 1064–1069, https://doi.org/10.1126/science.adf2983, 2023.

DeMott, C. A. and Randall, D. A.: Observed variations of tropical convective available potential energy, Journal of Geophysical Research: Atmospheres, 109, https://doi.org/10.1029/2003jd003784, 2004.

Echevin, V., Colas, F., Espinoza-Morriberon, D., Vasquez, L., Anculle, T., and Gutierrez, D.: Forcings and Evolution of the 2017 Coastal El Niño Off Northern Peru and Ecuador, Frontiers in Marine Science, 5, https://doi.org/10.3389/fmars.2018.00367, 2018.

Emanuel, K. A.: Atmospheric convection, Oxford university press, 1994.

Emmenegger, T., Ahmed, F., Kuo, Y.-H., Xie, S., Zhang, C., Tao, C., and Neelin, J. D.: The physics behind precipitation onset bias in CMIP6 models: The pseudo-entrainment diagnostic and trade-offs between lapse rate and humidity, Journal of Climate, 37, 2013–2033, 2024.

Fernandez-Palomino, C. A., Hattermann, F. F., Krysanova, V., Lobanova, A., Vega-Jácome, F., Lavado, W., Santini, W., Aybar, C., and Bronstert, A.: A novel high-resolution gridded precipitation dataset for Peruvian and Ecuadorian watersheds: Development and hydrological evaluation, Journal of Hydrometeorology, 23, 309–336, 2022.

Gálvez, J. M.: The Gálvez-Davison Index (GDI), Weather Prediction Center, National Oceanic and Atmospheric Administration. Available at: Available at: https://www.wpc.ncep.noaa.gov/international/gdi/(accessed on December 04, 2025), 2016.

Garreaud, R. D.: A plausible atmospheric trigger for the 2017 coastal El Niño, International Journal of Climatology, 38, https://doi.org/10.1002/joc.5426, 2018.

George, J. J.: Weather forecasting for aeronautics, Academic press, 2014.

Hersbach, H., Bell, B., Berrisford, P., Hirahara, S., Horányi, A., Muñoz-Sabater, J., Nicolas, J., Peubey, C., Radu, R., Schepers, D., Simmons, A., Soci, C., Abdalla, S., Abellan, X., Balsamo, G., Bechtold, P., Biavati, G., Bidlot, J., Bonavita, M., De Chiara, G., Dahlgren, P., Dee, D., Diamantakis, M., Dragani, R., Flemming, J., Forbes, R., Fuentes, M., Geer, A., Haimberger, L., Healy, S., Hogan, R. J., Hólm, E., Janisková, M., Keeley, S., Laloyaux, P., Lopez, P., Lupu, C., Radnoti, G., de Rosnay, P., Rozum, I., Vamborg, F., Villaume, S., and Thépaut,

J.: The ERA5 global reanalysis, Quarterly Journal of the Royal Meteorological Society, 146, 1999–2049, https://doi.org/10.1002/qj.3803, 2020.

Houze, R. A.: Mesoscale convective systems, Reviews of Geophysics, 42, https://doi.org/10.1029/2004rg000150, 2004.

John, V. and Soden, B.: Temperature and humidity biases in global climate models and their impact on climate feedbacks, Geophysical Research Letters, 34, 2007.

Lau, K.-M., Wu, H.-T., and Bony, S.: The Role of Large-Scale Atmospheric Circulation in the Relationship between Tropical Convection and Sea Surface Temperature, Journal of Climate, 10, 381–392, https://doi.org/10.1175/1520-0442(1997)010<0381:trolsa>2.0.co;2, 1997.

McPhaden, M. J., Zebiak, S. E., and Glantz, M. H.: ENSO as an Integrating Concept in Earth Science, Science, 314, 1740–1745, https://doi.org/10.1126/science.1132588, 2006.

Paek, H., Yu, J., and Qian, C.: Why were the 2015/2016 and 1997/1998 extreme El Niños different?, Geophysical Research Letters, 44, 1848–1856, https://doi.org/10.1002/2016gl071515, 2017.

Peng, Q., Xie, S.-P., Passalacqua, G. A., Miyamoto, A., and Deser, C.: The 2023 extreme coastal El Niño: Atmospheric and air-sea coupling mechanisms, Science Advances, 10, https://doi.org/10.1126/sciadv.adk8646, 2024.

Poveda, G., Waylen, P. R., and Pulwarty, R. S.: Annual and inter-annual variability of the present climate in northern South America and southern Mesoamerica, Palaeogeography, Palaeoclimatology, Palaeoecology, 234, 3–27, 2006.

Poveda, G., Mejia, J. F., Arias, P. A., Zuluaga, M. D., Salazar, J. F., Carmona, A. M., Builes-Jaramillo, A., Salas, H. D., Yepes, J., Martinez, J. A., and Bedoya-Soto, J. M.: Climate of Northwestern South America, https://doi.org/10.1093/acrefore/9780190228620.013.966, 2025.

Riehl, H.: On the heat balance in the equatorial trough zone, Geophysica, 6, 503–538, 1958.

Rivas Quispe, P. R., Anderson-Frey, A., and Mcmurdie, L. A.: An index for precipitation on the north coast of Peru using logistic regression, Atmósfera, 38, 2024.

Rodríguez-Morata, C., Díaz, H. F., Ballesteros-Canovas, J. A., Rohrer, M., and Stoffel, M.: The anomalous 2017 coastal El Niño event in Peru, Climate Dynamics, 52, 5605–5622, https://doi.org/10.1007/s00382-018-4466-y, 2018.

Rudloff, D., Lübbecke, J. F., and Wahl, S.: Seasonality of feedback mechanisms involved in Pacific coastal Niño events, Climate Dynamics, 63, 58, 2025.

Sanabria, J., Carrillo, C. M., and Labat, D.: Unprecedented Rainfall and Moisture Patterns during El Niño 2016 in the Eastern Pacific and Tropical Andes: Northern Perú and Ecuador, Atmosphere, 10, 768, https://doi.org/10.3390/atmos10120768, 2019.

Showalter, A. K.: A stability index for thunderstorm forecasting, Bulletin of the American Meteorological Society, 34, 250–252, 1953.

Sobel, A. H. and Bretherton, C. S.: Modeling tropical precipitation in a single column, Journal of climate, 13, 4378–4392, 2000.

Sulca, J.: Evidence of nonlinear Walker circulation feedbacks on extreme El Niño Pacific diversity: Observations and CMIP5 models, International Journal of Climatology, 41, 2934–2961, 2021.

Sulca, J. and Takahashi, K.: Forecasting austral summer precipitation along the western coast of South America (WCSA), Environmental Research Communications, 7, 101 005, https://doi.org/10.1088/2515-7620/ae0de9, 2025.

Sulca, J., Takahashi, K., Espinoza, J., Vuille, M., and Lavado-Casimiro, W.: Impacts of different<scp>ENSO</scp>flavors and tropical Pacific convection variability (<scp>ITCZ</scp>,<scp>SPCZ</scp>) on austral summer rainfall in South America, with a focus on Peru, International Journal of Climatology, 38, 420–435, https://doi.org/10.1002/joc.5185, 2017.

Takahashi, K.: The atmospheric circulation associated with extreme rainfall events in Piura, Peru, during the 1997–1998 and 2002 El Niño events, in: Annales Geophysicae, vol. 22, pp. 3917–3926, Copernicus GmbH, 2004.

Takahashi, K. and Dewitte, B.: Strong and moderate nonlinear El Niño regimes, Climate dynamics, 46, 1627–1645, 2016.

Takahashi, K. and Martínez, A. G.: The very strong coastal El Niño in 1925 in the far-eastern Pacific, Climate Dynamics, 52, 7389–7415, https://doi.org/10.1007/s00382-017-3702-1, 2017.

Takahashi, K., Montecinos, A., Goubanova, K., and Dewitte, B.: ENSO regimes: Reinterpreting the canonical and Modoki El Niño, Geophysical research letters, 38, 2011.

Takahashi, K., Aliaga-Nestares, V., Avalos, G., Bouchon, M., Castro, A., Cruzado, L., Dewitte, B., Gutiérrez, D., Lavado-Casimiro, W., Marengo, J., et al.: The 2017 coastal el nino, https://doi. org/10.1175/2018BAMSStateoftheClimate. 1, 2018.

Thielen, D. R., Ramoni-Perazzi, P., Zamora-Ledezma, E., Puche, M. L., Marquez, M., Quintero, J. I., Rojas, W., Quintero, A., Bianchi, G., Soto-Werschitz, I. A., and Arizapana-Almonacid, M. A.: Effect of extreme El Niño events on the precipitation of Ecuador, Natural Hazards and Earth System Sciences, 23, 1507–1527, https://doi.org/10.5194/nhess-23-1507-2023, 2023.

Trenberth, K. E.: The definition of el nino, Bulletin of the American Meteorological Society, 78, 2771–2778, 1997.

Wang, C., Deser, C., Yu, J.-Y., DiNezio, P., and Clement, A.: El Niño and Southern Oscillation (ENSO): A Review, p. 85–106, Springer Netherlands, ISBN 9789401774994, https://doi.org/10.1007/978-94-017-7499-4_4, 2016.

Williams, E. and Renno, N.: An Analysis of the Conditional Instability of the Tropical Atmosphere, Monthly Weather Review, 121, 21–36, https://doi.org/10.1175/1520-0493(1993)121<0021:aaotci>2.0.co;2, 1993.

Yu, H. and Zhang, M.: Explaining the year-to-year variability of the Eastern Pacific intertropical convergence zone in the boreal spring, Journal of Geophysical Research: Atmospheres, 123, 3847–3856, 2018.

Zipser, E. J.: Some Views On “Hot Towers” after 50 Years of Tropical Field Programs and Two Years of TRMM Data, Meteorological Monographs, 29, 49–49, https://doi.org/10.1175/0065-9401(2003)029<0049:csvoht>2.0.co;2, 2003.

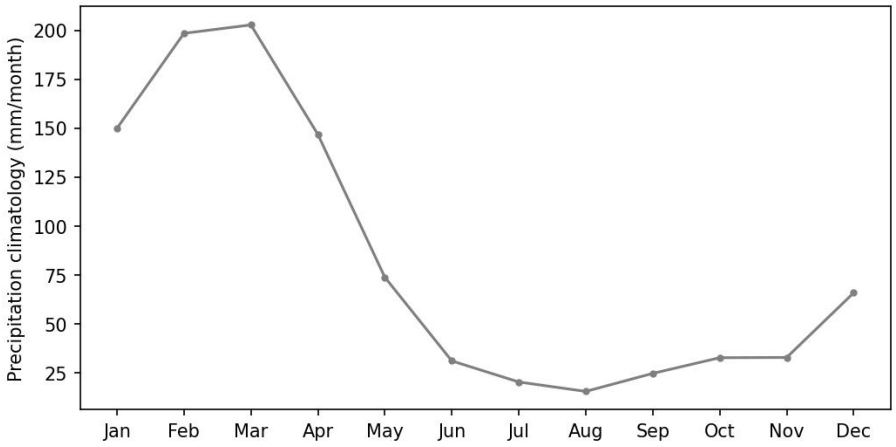

Figure 1. Precipitation climatology as the 1981-2015 median from ERA5 averaged over the NWSA next to 1+2 El Niño region.

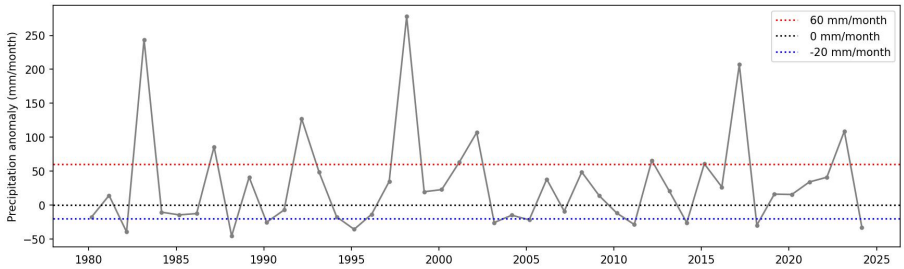

Figure 2. Monthly precipitation anomaly in March from ERA5, taking the 1981-2015 median as climatology, averaged over the NWSA next to 1+2 El Niño region. Points above (below) horizontal red (blue) dotted line are considered as rainiest (driest) events.

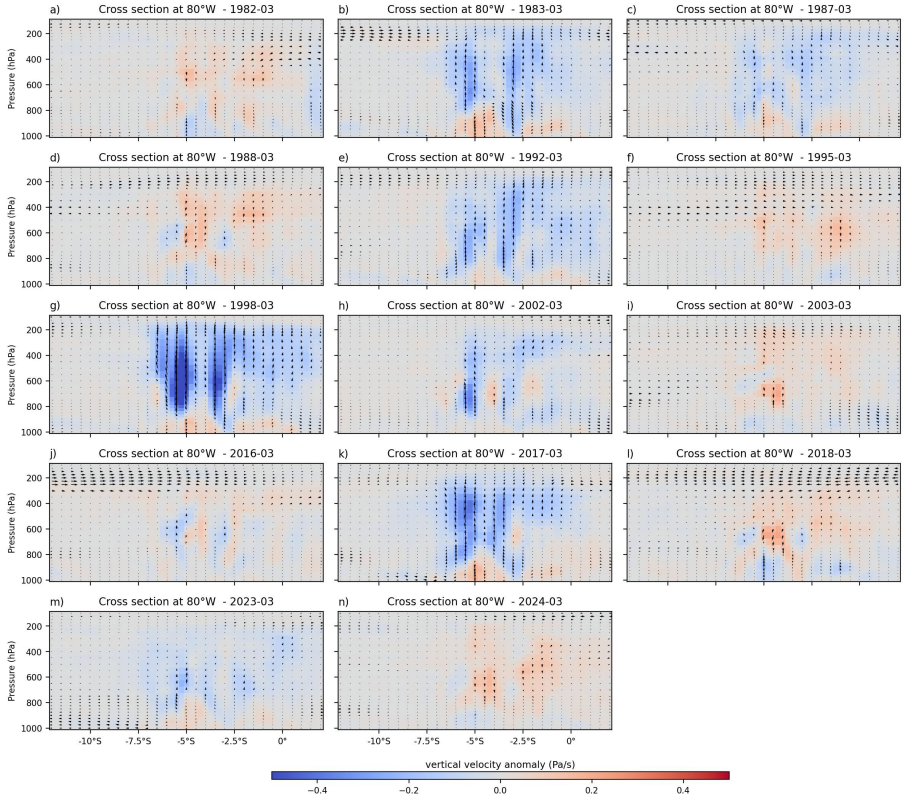

Figure 3. Latitudinal cross-section of the resultant vector between the anomalies of ω and meridional wind at 80°W for the rainiest and driest events identified in Section 4. The blue (red) shaded colors indicate negative (positive) values of ω. The ω vector was multiplied by -20 to increase its scale and to get upward (downward) arrows with the air ascent (descent). Anomalies were calculated taking the 1981-2015 median as climatology.

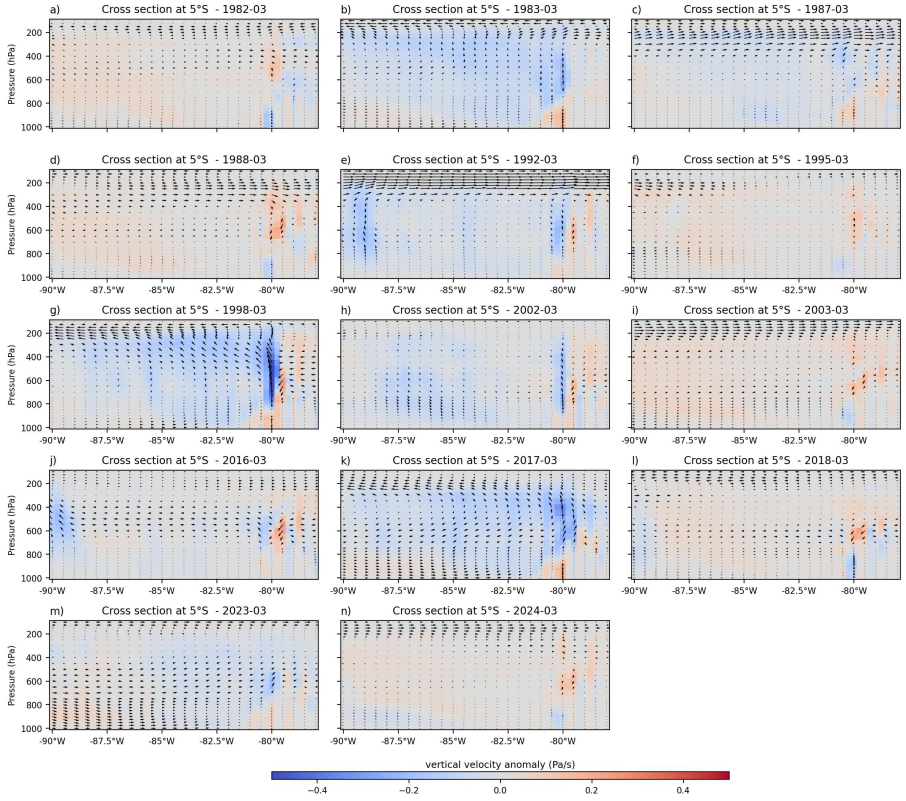

Figure 4. Longitudinal cross-section of the resultant vector between the anomalies of ω and zonal wind at 5°S for the rainiest and driest events identified in Section 4. The blue (red) shaded colors indicate negative (positive) values of ω. The ω vector was multiplied by -20 to increase its scale and to get upward (downward) arrows with the air ascent (descent). Anomalies were calculated taking the 1981-2015 median as climatology.

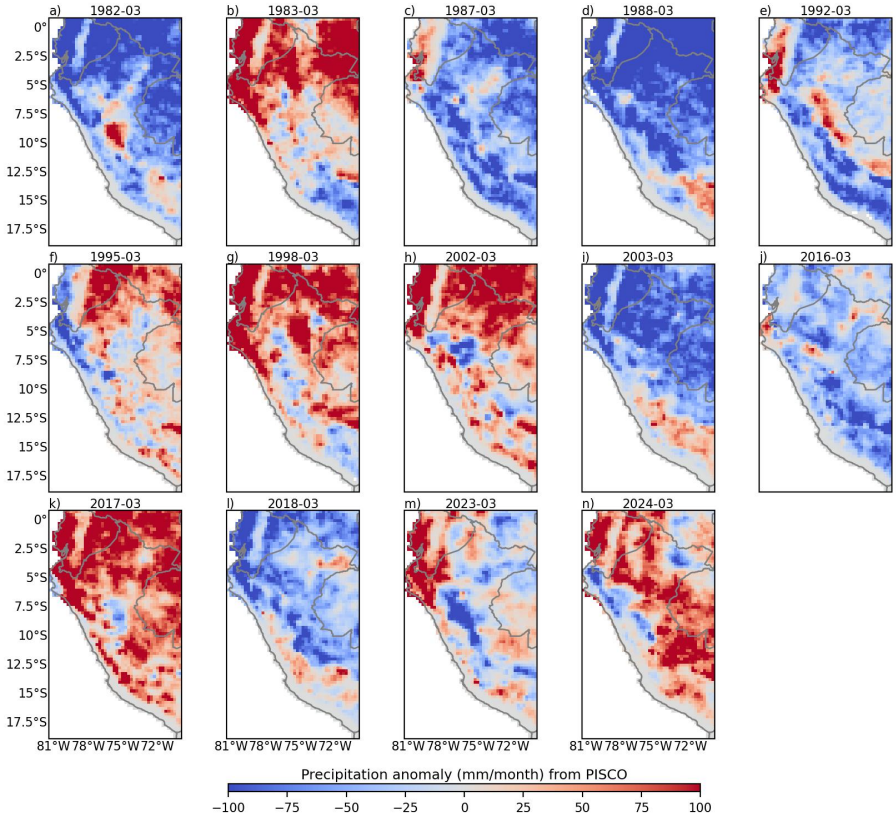

Figure 5. Precipitation anomaly, taking the 1981-2015 median as climatology, from PISCO for the rainiest and driest events identified in Section 4. The blue (red) shaded colors indicate negative (positive) values of precipitation.

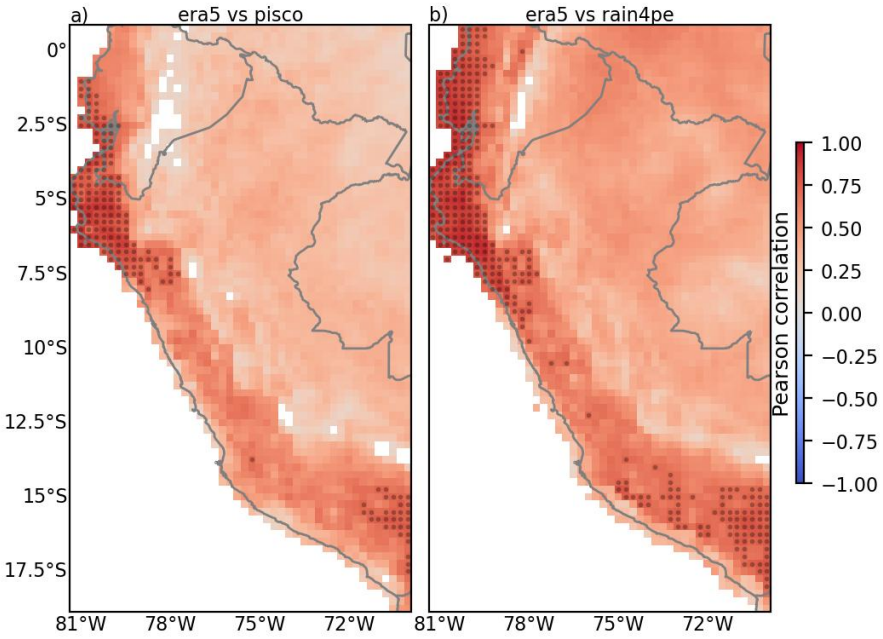

Figure 6. Pearson correlation (R) at the 95% confidence level between monthly precipitation anomaly from ERA5 and PISCO (a) for 1981-2024, and RAIN4PE (b) for 1981-2015. Only pixels with significant R (p-value<0.05) are shown, the gray points represent R>0.7. The blue (red) shaded colors indicate negative (positive) values of R. Anomalies were calculated taking the 1981-2015 median as climatology.

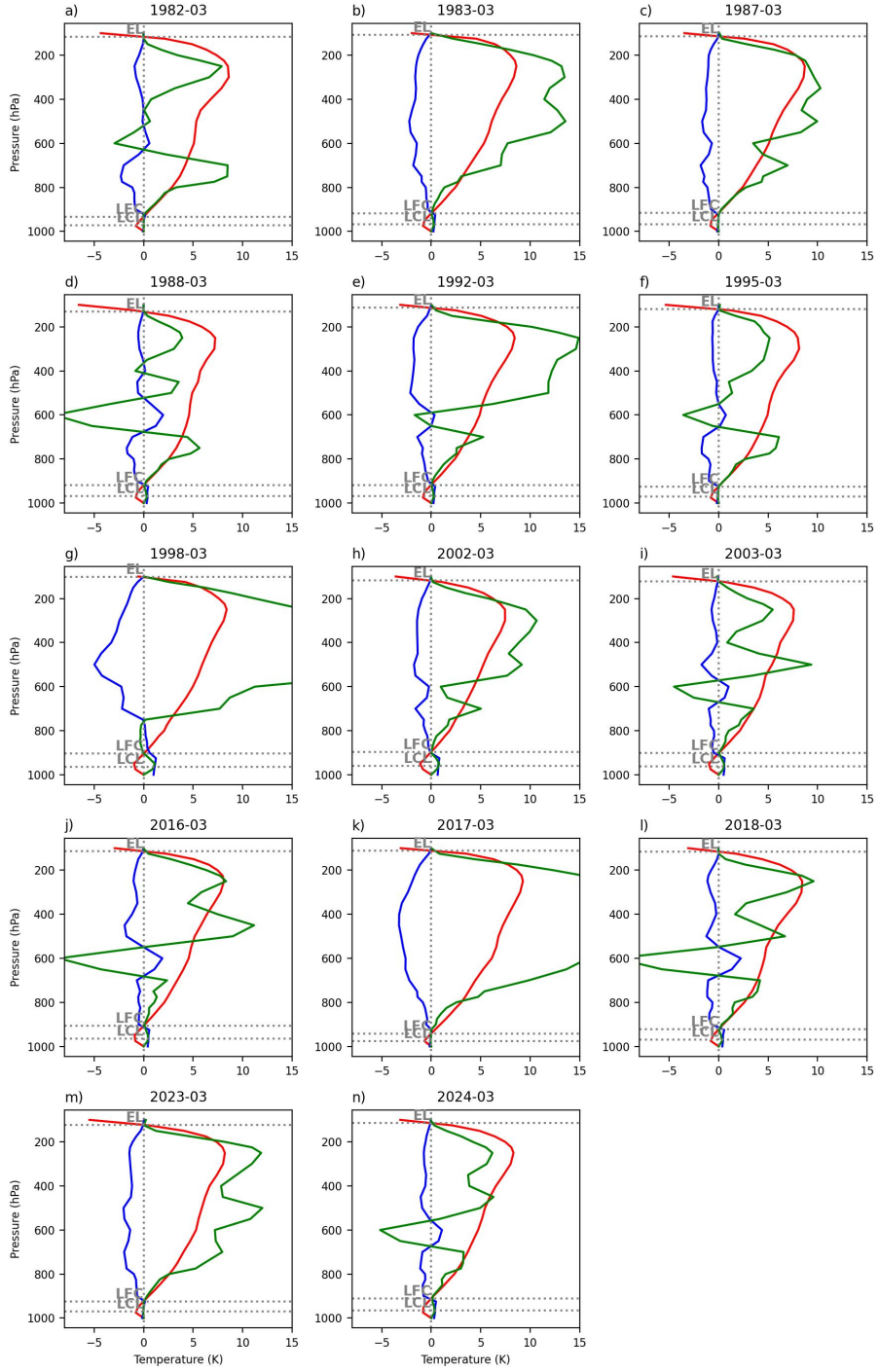

Figure 7. Profiles of ΔT (red), ω (blue) and $-\omega\Delta T$ (green) at (80°W,5°S) for the rainiest and driest events identified in Section 4. The LCL, LFC and EL dotted horizontal lines represent the lifting condensation level, the level of free convection and the equilibrium level respectively. The ω was multiplied by 10 to increase its scale.

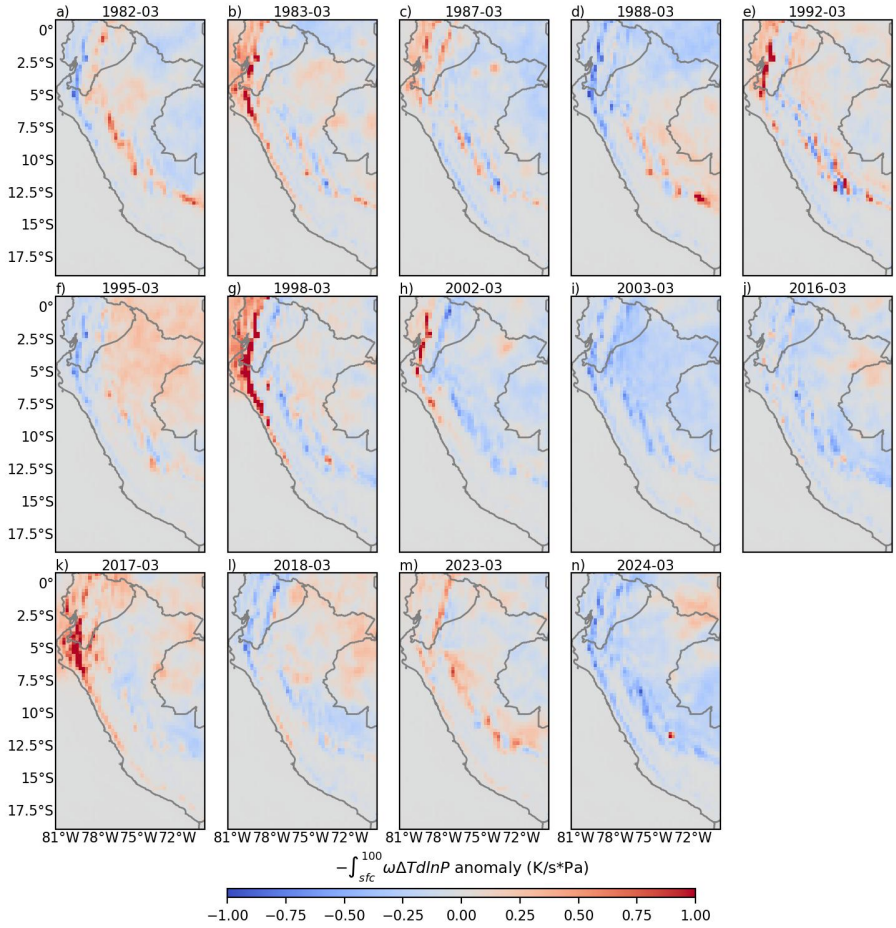

Figure 8. BWR anomaly, taking the 1981-2015 median as climatology, for the rainiest and driest events identified in Section 4. The blue (red) shaded colors indicate negative (positive) values of BWR. Positive (negative) values indicate favorable (unfavorable) conditions for deep convection.

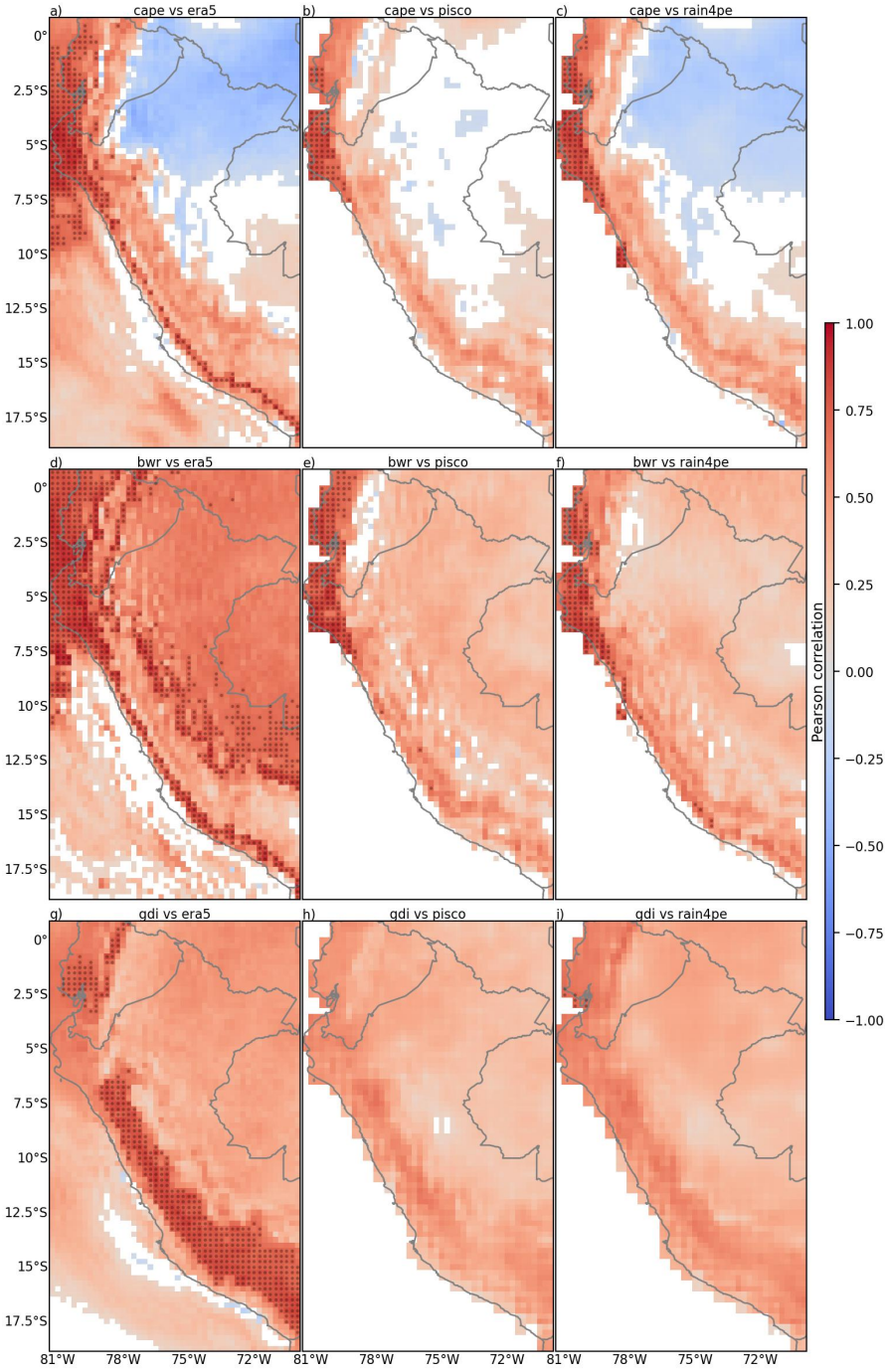

Figure 9. Pearson correlation (R) maps at the 95% confidence level between monthly anomalies of convective indices (rows) and precipitation datasets (columns) for the 1981-2015 common period. The indices (rows) are (a-c) CAPE, (d-f) BWR, (g-i) GDI, (h-l) Ia, and (m-o) Id. The precipitation datasets (columns) are (a, d, g) ERA5, (b, e, h) PISCO, and (c, f, i) RAIN4PE. Shading is shown only for significant correlations (p-value < 0.05). Red (blue) indicates positive (negative) R values. Gray points highlight strong correlations (R > 0.7). Anomalies were calculated taking the 1981-2015 median as climatology.

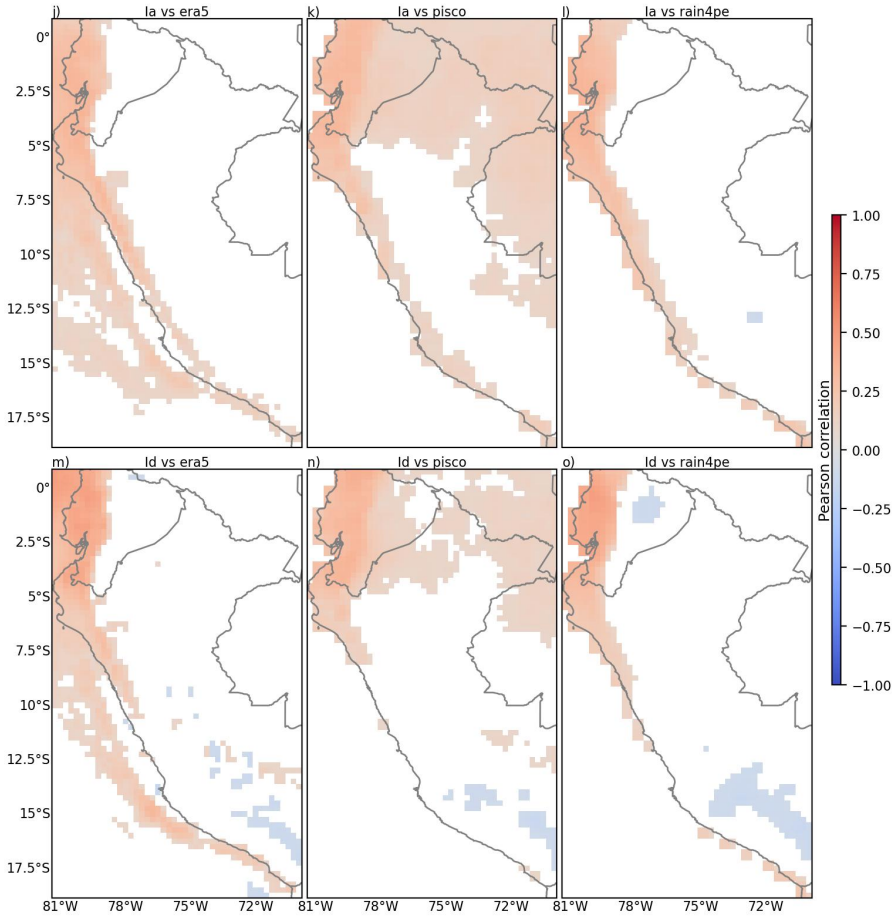

Figure 9. (Continued).

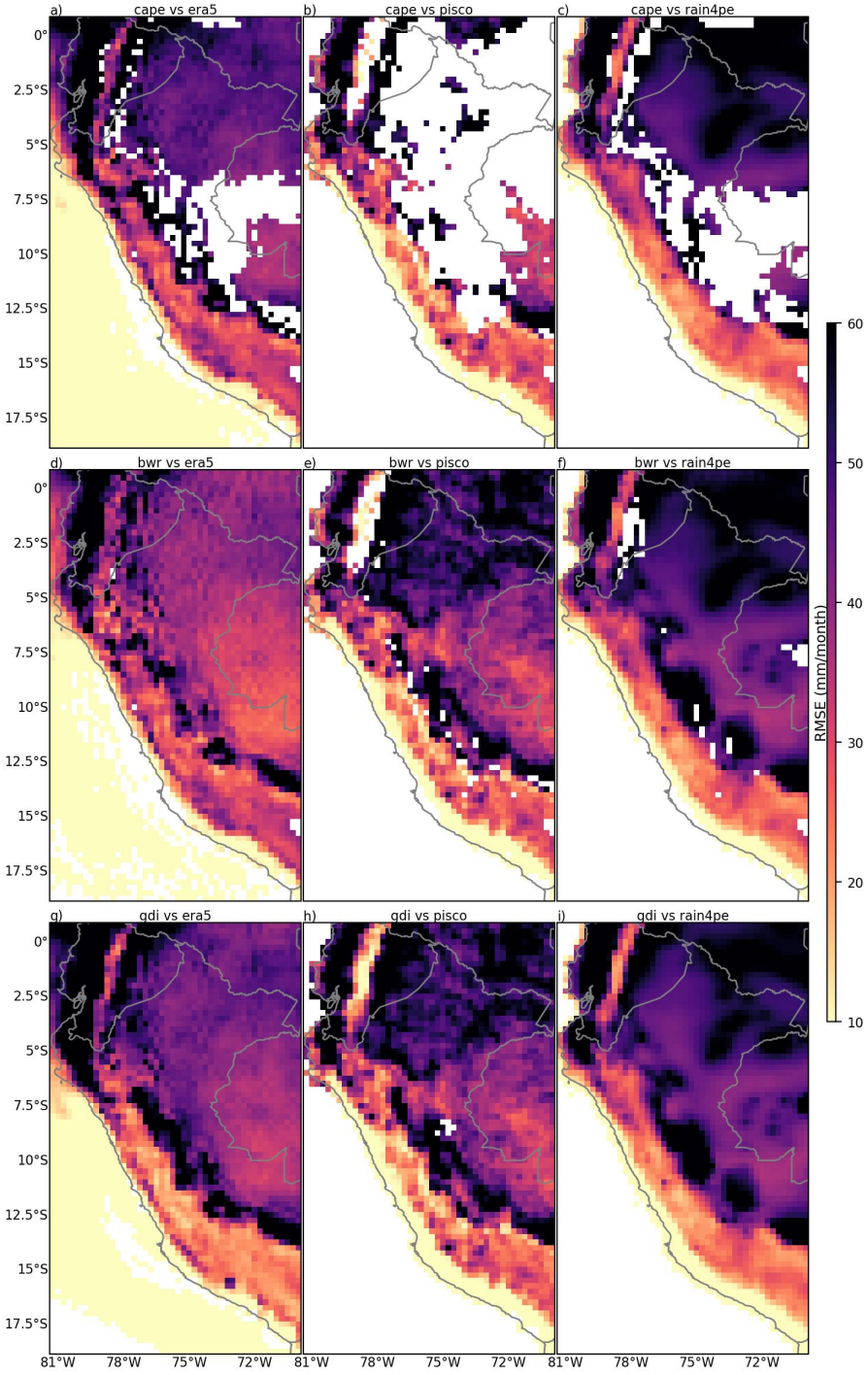

Figure 10. Spatial distribution of RMSE in mm month^{-1} for the common period 1981-2015. Anomaly precipitation was estimated using linear regression based on five convective indices: CAPE (a-c), BWR (d-f), GDI (g-i), (h-l) Ia, and (m-o) Id. The RMSE was calculated by comparing the estimates against three precipitation anomaly products: ERA5 (left column), PISCO (middle column), and RAIN4PE (right column). Values are only displayed for pixels with a significant regression ($p < 0.05$).

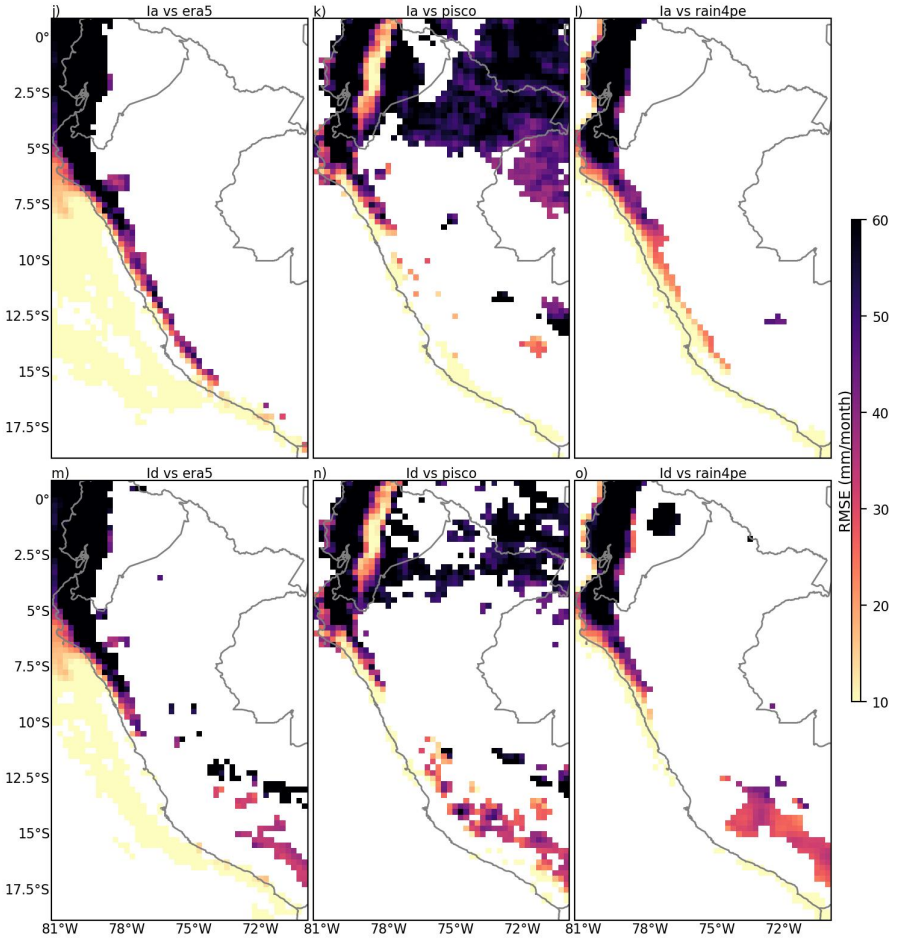

Figure 10. (Continued).

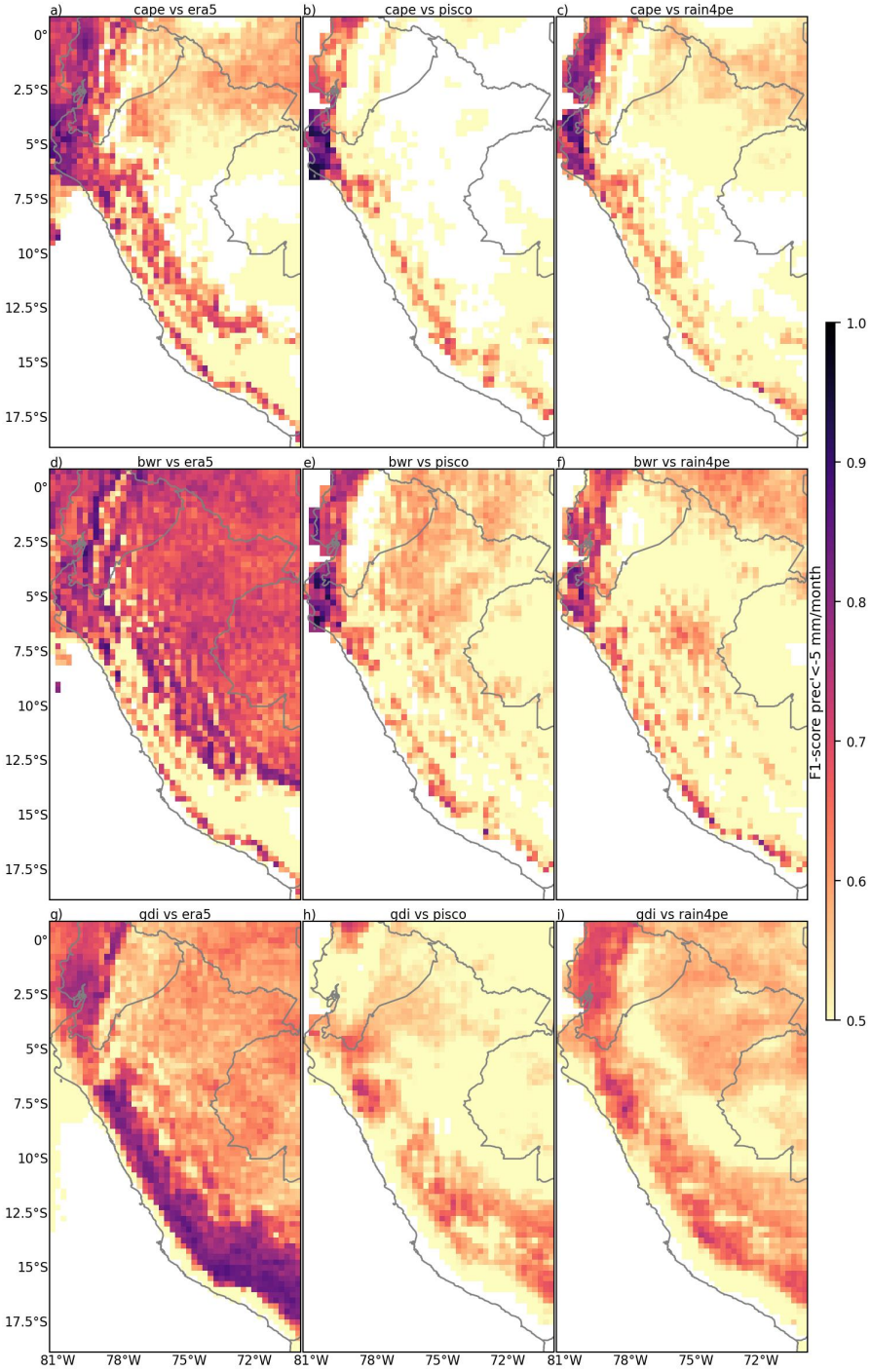

Figure 11. Spatial distribution of F1-score for precipitation anomalies lower than -5 mm month^{-1}. Precipitation was estimated using linear regression based on five convective indices: CAPE (a-c), BWR (d-f), GDI (g-i), (h-l) Ia, and (m-o) Id. The F1-score was calculated by validating the estimates against three precipitation anomaly products: ERA5 (left column), PISCO (middle column), and RAIN4PE (right column). Values are only displayed for pixels with a significant regression ($p < 0.05$).

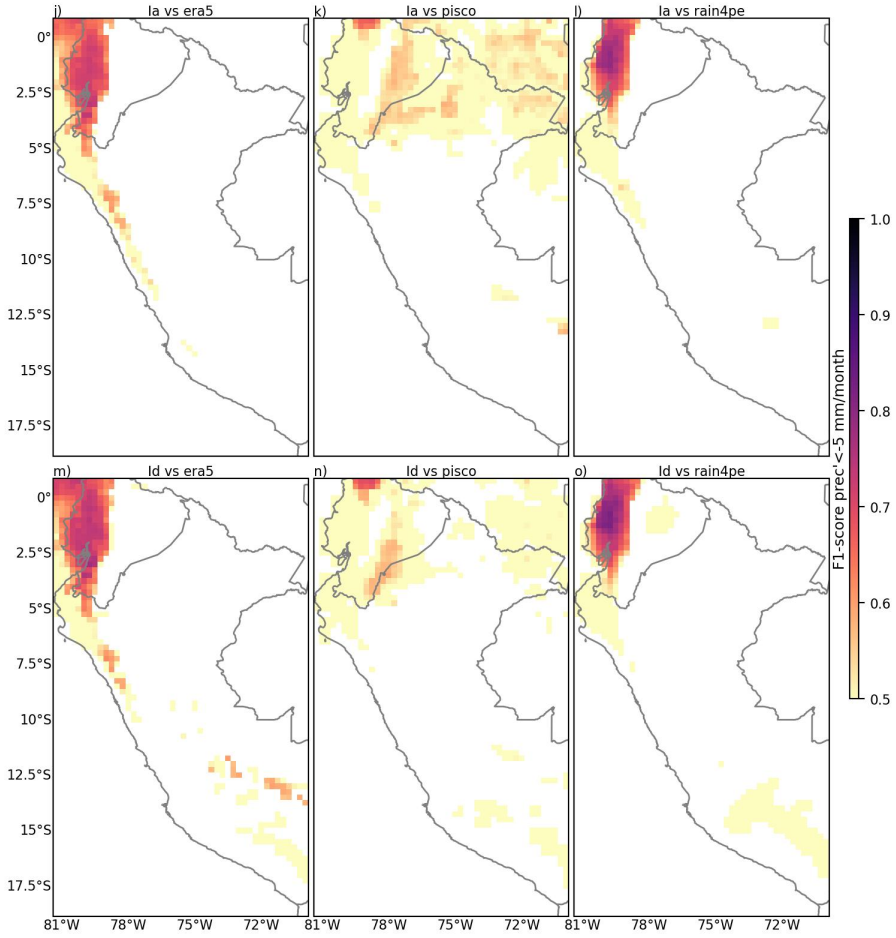

Figure 11. (Continued).

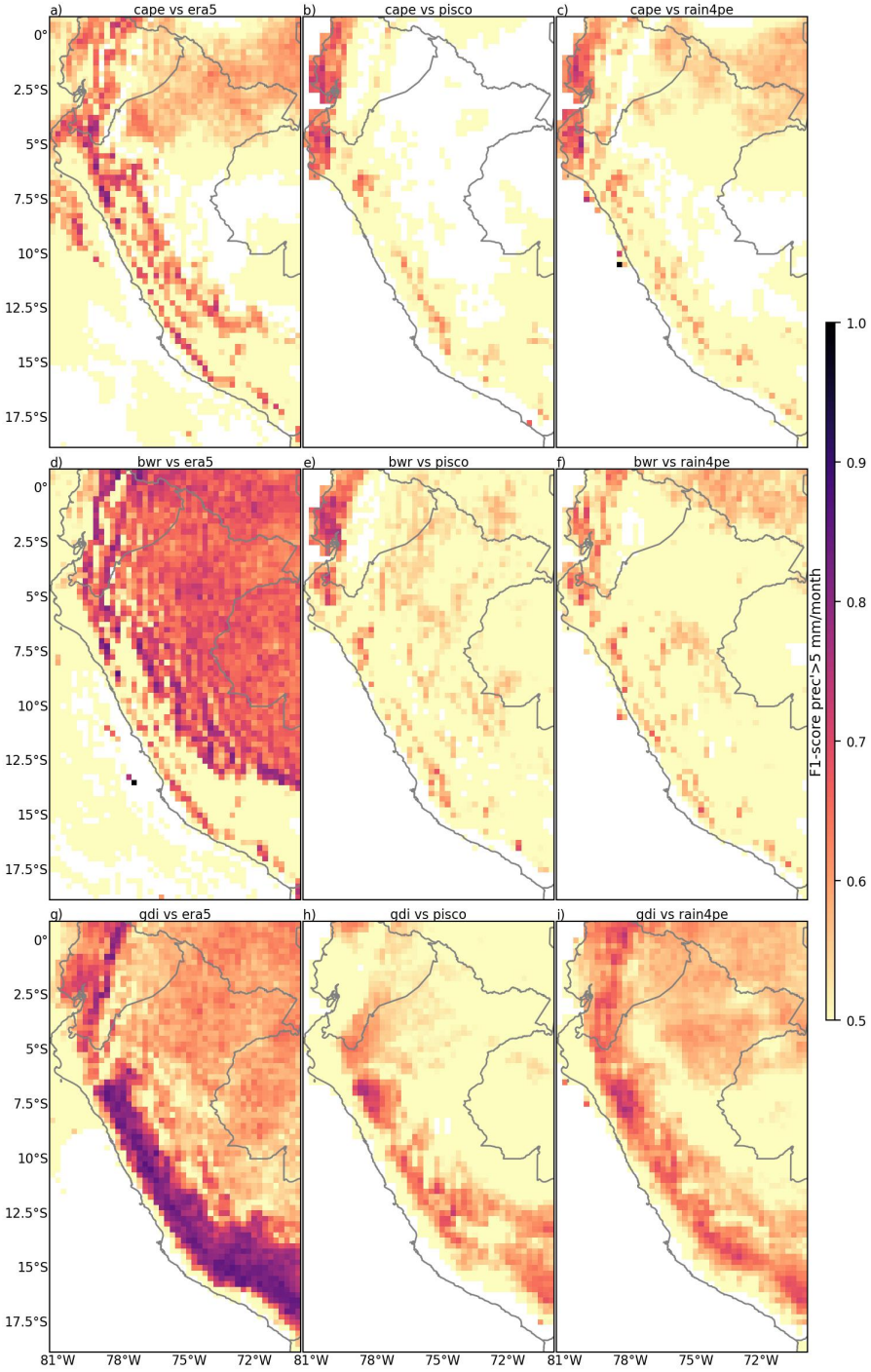

Figure 12. Same as Fig.11, but the F1-score was calculated for precipitation anomalies greater than 5 mm month^{-1}.

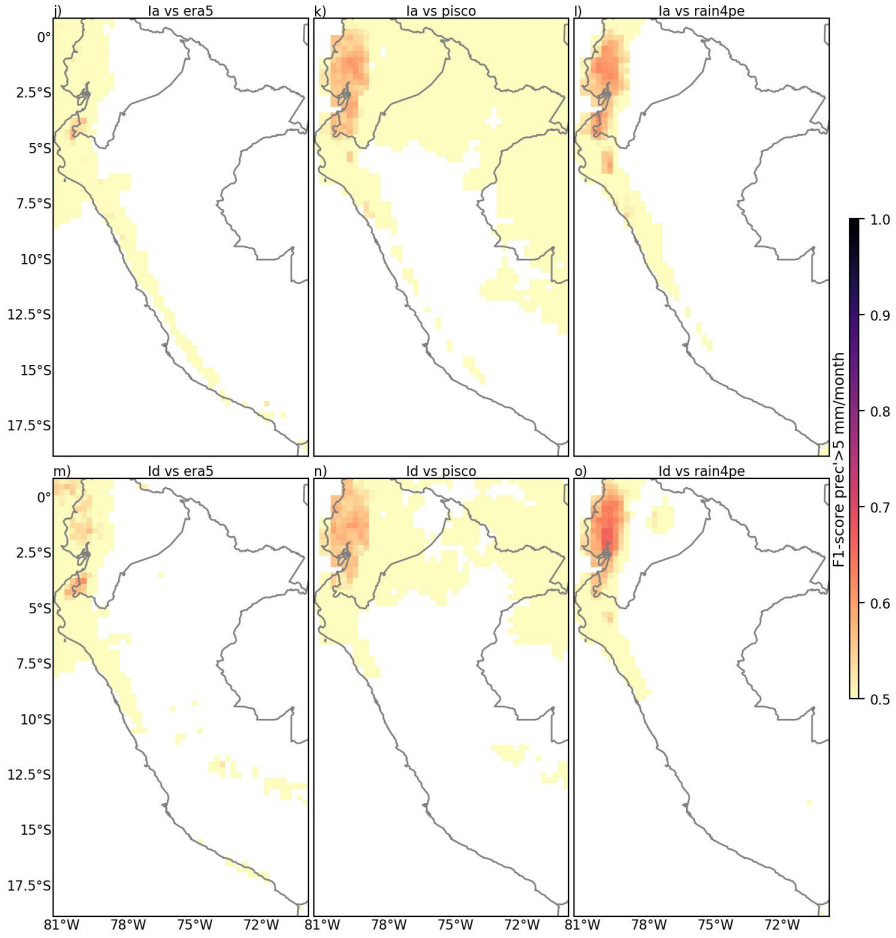

Figure 12. (Continued).

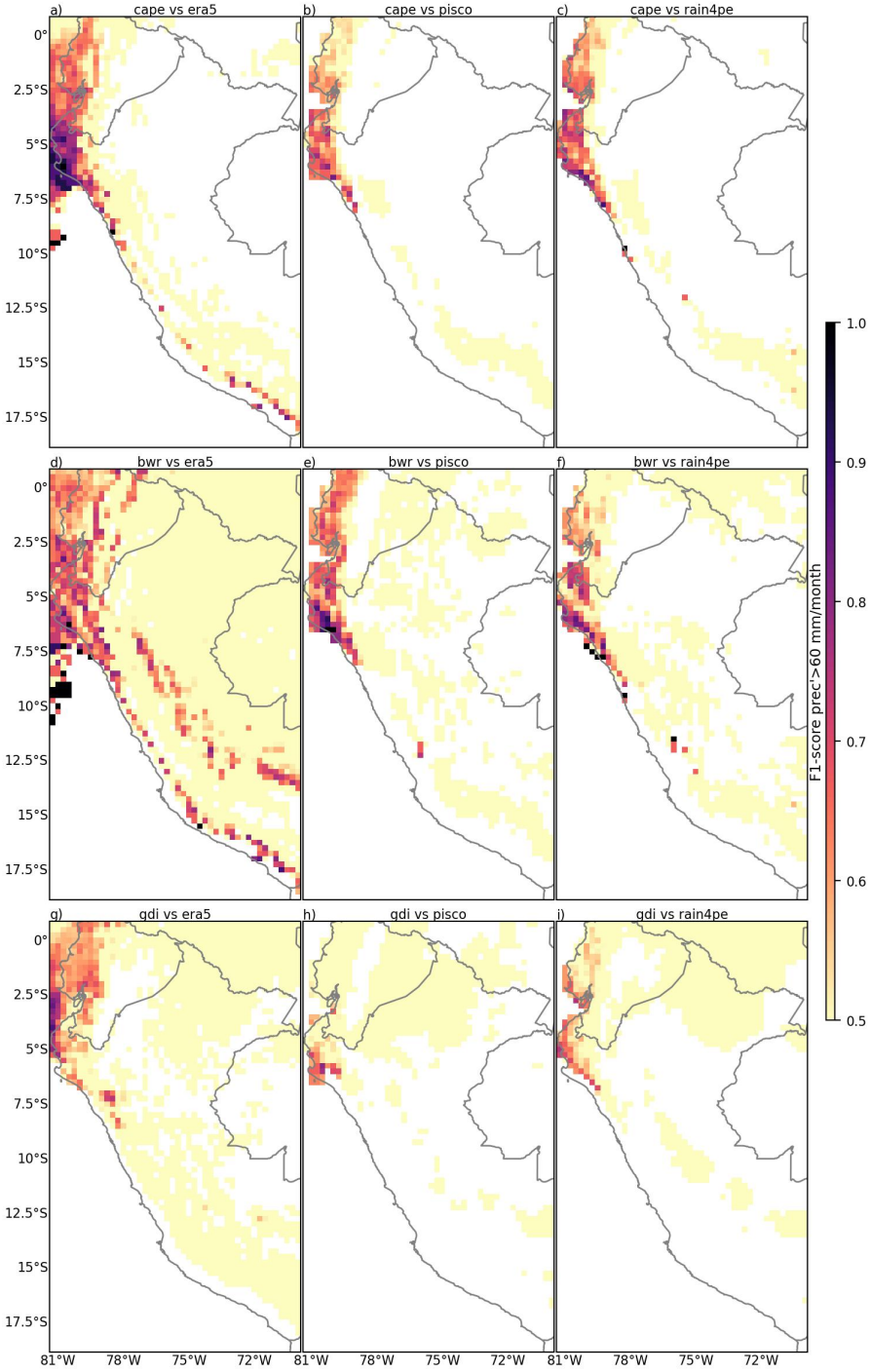

Figure 13. Same as Fig.11, but the F1-score was calculated for precipitation anomalies greater than 60 mm month^{-1}.

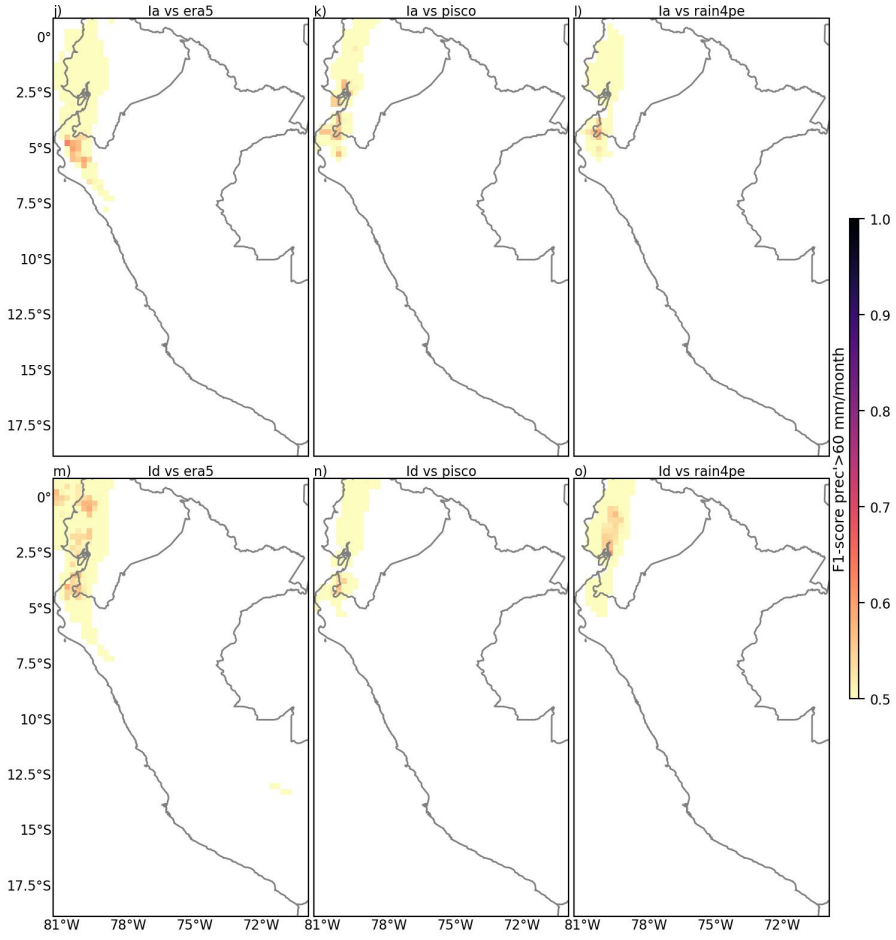

Figure 13. (Continued).

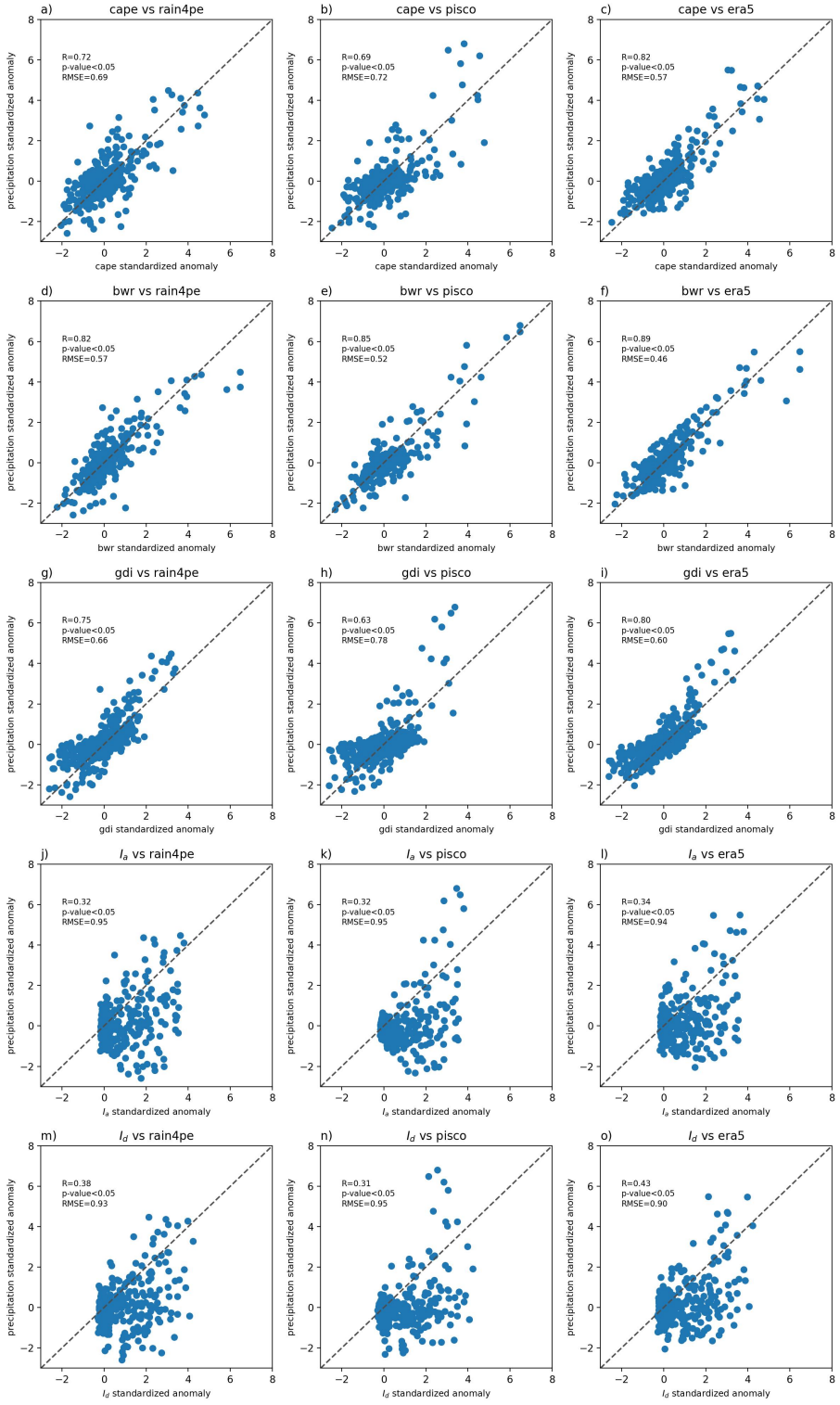

Figure 14. Scatterplots between convective indices and precipitation datasets over the NWSA adjacent to Niño 1+2. Scatterplots comparing monthly standardized anomalies of CAPE (a-c), BWR (d-f), GDI (g-i), (h-l) Ia, and (m-o) Id against standardized precipitation anomalies from ERA5 (left column), PISCO (middle column), and RAIN4PE (right column). All data are spatially averaged over the NWSA adjacent to Niño 1+2. The Pearson correlation coefficient (R), RMSE and the significance at the 95% confidence level (p-value < 0.05) are shown in

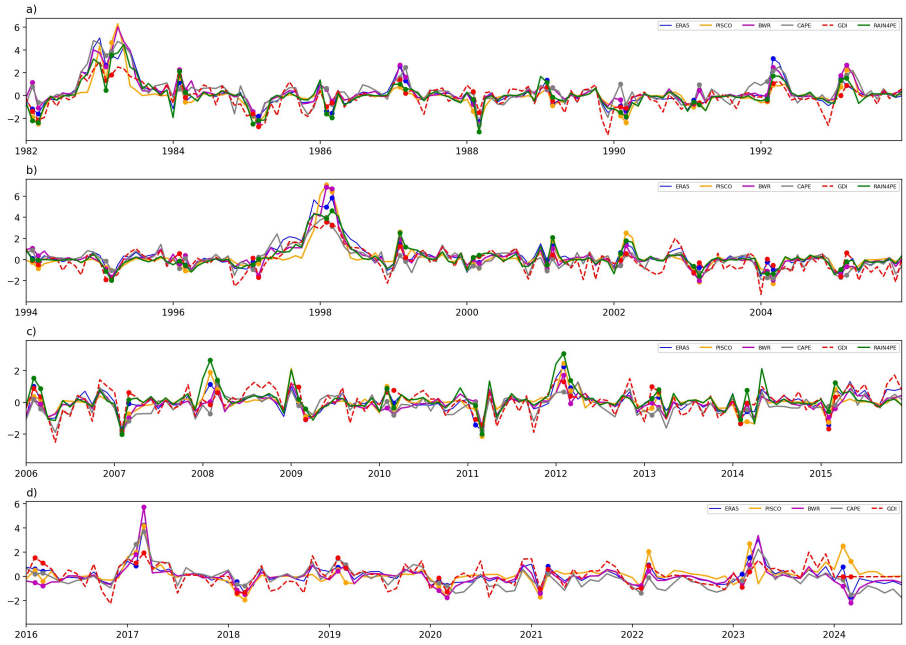

Figure 15. Time series of monthly standardized anomalies of convective indices, such as CAPE (gray), BWR (magenta), and GDI (dashed red), and standardized precipitation from ERA5 (blue), PISCO (orange), and RAIN4PE (green). All data are spatially averaged over the NWSA adjacent to Niño 1+2 for the period 1981-2024. The RAIN4PE dataset is only available for 1981-2015. Anomalies were calculated taking the 1981-2015 median as climatology. Circle markers indicate February and March of every year.

Appendix A

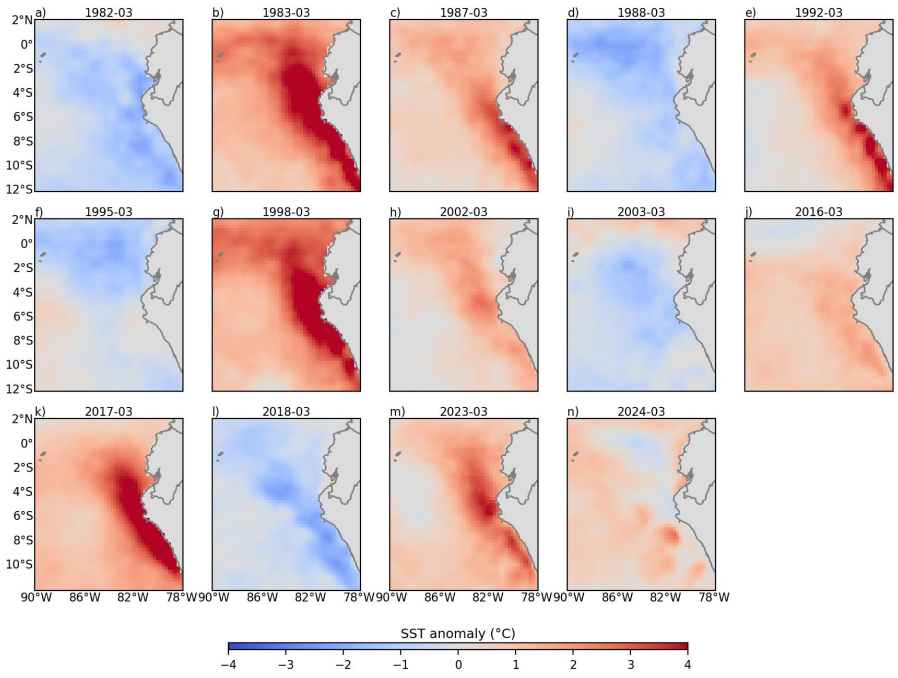

Figure A1. SST anomaly from ERA5 for the rainiest and driest events identified in Section 4 over the Niño 1+2 region. The blue (red) shaded colors indicate negative (positive) values of SST.

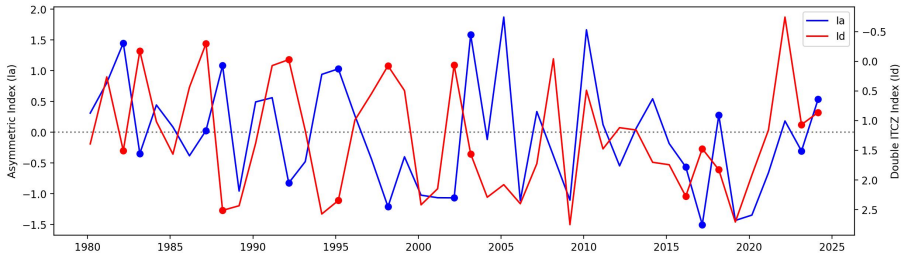

Figure A2. Time series of the March Ia and Id indices for the period 1981-2024 taking the same areas proposed by Aliaga-Nestares et al. (2023).

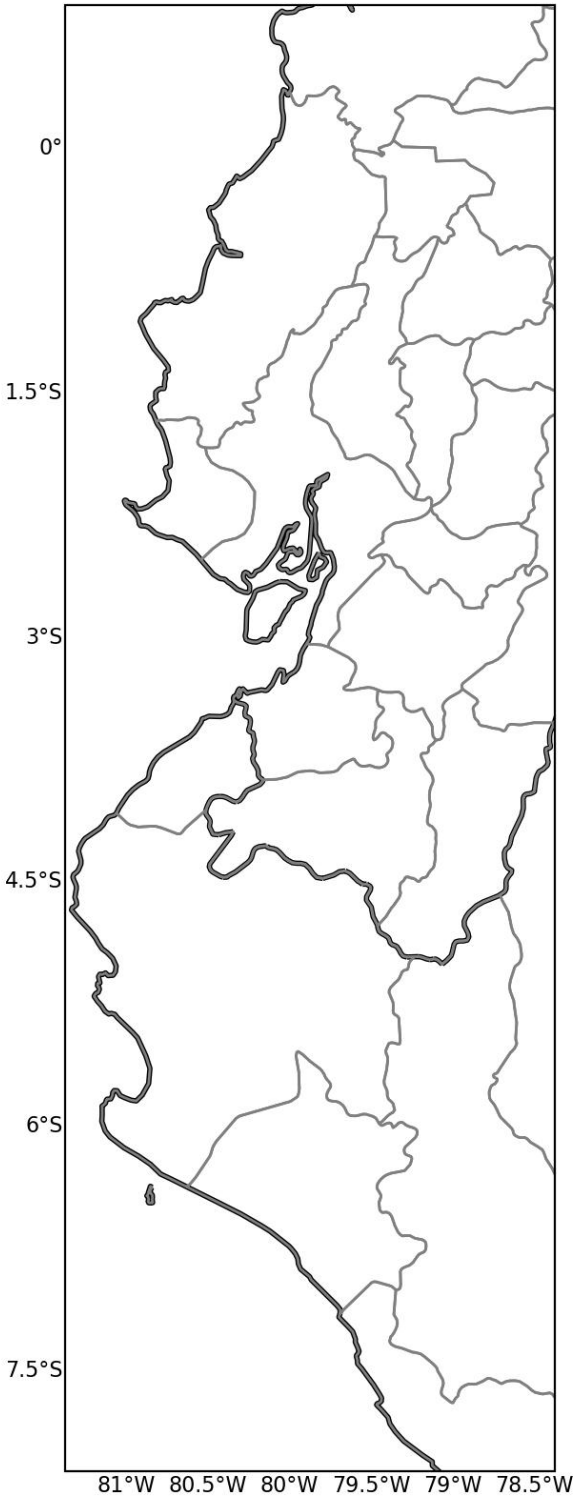

Figure A3. NWSA adjacent to Niño 1+2 area (81.25°W-78.5°W, 8°S-0.75°N).